Monthly Notices
of the
ROYAL ASTRONOMICAL SOCIETY

MNRAS **513,** 2904–2929 (2022) https://doi.org/10.1093/mnras/stac818
Advance Access publication 2022 March 24

H α emission in local galaxies: star formation, time variability, and the diffuse ionized gas

Sandro Tacchella,[1,2,3,4]★ Aaron Smith,[5]★† Rahul Kannan,[2]★ Federico Marinacci,[6]
Lars Hernquist,[2] Mark Vogelsberger,[5] Paul Torrey,[7] Laura Sales[8] and Hui Li[9]‡

[1]*Department of Physics, Ulsan National Institute of Science and Technology (UNIST), Ulsan 44919, Republic of Korea*
[2]*Center for Astrophysics | Harvard & Smithsonian, 60 Garden St, Cambridge, MA 02138, USA*
[3]*Kavli Institute for Cosmology, University of Cambridge, Madingley Road, Cambridge, CB3 0HA, UK*
[4]*Cavendish Laboratory, University of Cambridge, 19 JJ Thomson Avenue, Cambridge, CB3 0HE, UK*
[5]*Department of Physics, Massachusetts Institute of Technology, Cambridge, MA 02139, USA*
[6]*Department of Physics and Astronomy 'Augusto Righi', University of Bologna, via Gobetti 93/2, I-40129 Bologna, Italy*
[7]*Department of Astronomy, University of Florida, 211 Bryant Space Sciences Center, Gainesville, FL 32611, USA*
[8]*Department of Physics and Astronomy, University of California, Riverside, 900 University Avenue, Riverside, CA 92521, USA*
[9]*Department of Astronomy, Columbia University, New York, NY 10027, USA*

Accepted 2022 March 21. Received 2022 March 17; in original form 2021 November 30

ABSTRACT

The nebular recombination line H α is widely used as a star formation rate (SFR) indicator in the local and high-redshift Universe. We present a detailed H α radiative transfer study of high-resolution isolated Milky-Way and Large Magellanic Cloud simulations that include radiative transfer, non-equilibrium thermochemistry, and dust evolution. We focus on the spatial morphology and temporal variability of the H α emission, and its connection to the underlying gas and star formation properties. The H α and H β radial and vertical surface brightness profiles are in excellent agreement with observations of nearby galaxies. We find that the fraction of H α emission from collisional excitation amounts to $f_{\rm col} \sim 5$–10 per cent, only weakly dependent on radius and vertical height, and that scattering boosts the H α luminosity by ~ 40 per cent. The dust correction via the Balmer decrement works well (intrinsic H α emission recoverable within 25 per cent), though the dust attenuation law depends on the amount of attenuation itself both on spatially resolved and integrated scales. Important for the understanding of the H α–SFR connection is the dust and helium absorption of ionizing radiation (Lyman continuum [LyC] photons), which are about $f_{\rm abs} \approx 28$ per cent and $f_{\rm He} \approx 9$ per cent, respectively. Together with an escape fraction of $f_{\rm esc} \approx 6$ per cent, this reduces the available budget for hydrogen line emission by nearly half ($f_{\rm H} \approx 57$ per cent). We discuss the impact of the diffuse ionized gas, showing – among other things – that the extraplanar H α emission is powered by LyC photons escaping the disc. Future applications of this framework to cosmological (zoom-in) simulations will assist in the interpretation of spectroscopy of high-redshift galaxies with the upcoming *James Webb Space Telescope*.

Key words: radiative transfer – H II regions – ISM: structure – galaxies: star formation.

1 INTRODUCTION

The Balmer lines are some of the most utilized and observed emission lines in astrophysics since they are in the optical and relatively ubiquitous as they arise from recombination to the $n = 2$ level of hydrogen, the most common element. In particular, the H α emission line is one of the prime indicators for the star formation rate (SFR) of and within galaxies as H α traces the ionized gas of star-forming H II regions. H α is used to measure the SFRs locally and out to redshift of $z \sim 2.5$ both on global (Kennicutt 1983; Lee et al. 2009; Koyama et al. 2015; Shivaei et al. 2015) and spatially resolved scales (e.g. Tacchella et al. 2015, 2018; Nelson et al. 2016b; Belfiore et al. 2018; Ellison et al. 2018). The upcoming *James Webb Space Telescope* (*JWST*) will extend this redshift limit to $z \sim 7$. Furthermore, H α is frequently used to shed light on the variability of the star-formation activity in galaxies since it traces younger stars than other SFR tracers such as the UV continuum (e.g. Weisz et al. 2012; Guo et al. 2016; Caplar & Tacchella 2019; Faisst et al. 2019; Haydon et al. 2020b).

Although H α is a well-calibrated SFR tracer (e.g. Shivaei et al. 2015), uncertainties remain due to dust attenuation and emission from non-H II regions. In principle, one can derive the amount of dust attenuation of H α ($A_{\rm H\alpha}$) from the difference of the observed H α/H β ratio (i.e. the Balmer decrement) relative to the intrinsic H α/H β ratio, which itself only weakly depends on local conditions (i.e. electron density and temperature of the H II region) and therefore is well determined from first principles. Therefore, the Balmer decrement is the method of choice for correcting the observed H α emission for dust attenuation (Berman 1936; Calzetti, Kinney & Storchi-Bergmann 1994; Groves, Brinchmann & Walcher 2012;

★ E-mail: st578@cam.ac.uk (ST); arsmith@mit.edu (AS); rahul.kannan@cfa.harvard.edu (RK)
† NHFP Einstein Fellow.
‡ NHFP Hubble Fellow.

Nelson et al. 2016a), with the main uncertainty for estimating $A_{\mathrm{H}\alpha}$ arising from the adopted attenuation law.

In addition to aforementioned H II regions, diffuse ionized gas (DIG; sometimes also called the warm ionized gas) can also emit H α. Narrow-band H α imaging surveys suggest that the DIG emission contributes 20–60 per cent of the total H α flux in local spiral galaxies (Zurita, Rozas & Beckman 2000; Oey et al. 2007; Kreckel et al. 2016; Chevance et al. 2020) and therefore can bias H α-based SFRs as well as gas-phase metallicity estimates (e.g. Sanders et al. 2017; Poetrodjojo et al. 2019; Vale Asari et al. 2019). Furthermore, the DIG – as traced by H α – typically extends vertically above the plane of the disc to scales of about ∼1 kpc (Hoyle & Ellis 1963; Reynolds 1989; Rand, Kulkarni & Hester 1990; Jo et al. 2018; Levy et al. 2019). Two possibilities have been suggested for the origin of this diffuse, extraplanar H α emission. First, the extraplanar H α emission traces extraplanar DIG, which itself is produced by ionizing photons transported through transparent pathways carved out by superbubbles or chimneys (Mac Low & Ferrara 1999; Veilleux, Cecil & Bland-Hawthorn 2005). Secondly, the extraplanar H α emission is caused by dust scattering of the photons originating from H II regions in the galactic disc (Reynolds 1990; Ferrara et al. 1996).

Theoretically, it is still challenging to self-consistently model – on scales of entire galaxies – the detailed structure of the multiphase interstellar medium (ISM), including massive stars and supernovae in a radiation hydrodynamical context (Rosdahl & Teyssier 2015; Kannan et al. 2020; Vogelsberger et al. 2020). A handful of theoretical investigations have focused on the production and transport of H α photons (and similar emission lines, e.g. Katz et al. 2019; Wilkins et al. 2020) with various degrees of sophistication and self-consistency, e.g. while also contending with simulation resolution effects. Previous studies include an estimate of the importance of scattered light in the diffuse H α galactic background (Wood & Reynolds 1999; Barnes et al. 2015), an investigation of the star formation relation (without dust) from simulations of isolated dwarfs and high-redshift galaxies (Kim et al. 2013, 2019), sub-resolution population synthesis for a Milky-Way-like galaxy (Pellegrini et al. 2020a,b), and periodic tall box simulations to explore sub-parsec scale feedback and emission (Peters et al. 2017; Kado-Fong et al. 2020). Our work presented here further expands on this class of detailed emission line modelling. The novelty of our approach is that H α is self-consistently reprocessed from ionizing photons and that LyC and H α are self-consistently scattered/absorbed by dust throughout entire galaxies. In other words, H α is emitted from ionized/excited gas rather than assuming an SFR–H α conversion from H II regions from young star particles.

Specifically, in this paper we use the high-resolution Milky-Way (MW) and Large Magellanic Cloud (LMC) simulations from Kannan et al. (2020), which combines the state-of-the-art AREPO-RT code (Kannan et al. 2019) with a non-equilibrium thermochemistry module that accounts for molecular hydrogen (H_2) coupled to explicit dust formation and destruction. This is all integrated into a novel stellar feedback framework, the Stars and MUltiphase Gas in GaLaxiEs (SMUGGLE) feedback model (Marinacci et al. 2019). We employ the Cosmic Ly α Transfer code (COLT; Smith et al. 2015, 2019) to perform post-processing Monte Carlo radiative transfer (MCRT) calculations for ionizing radiation and Ly α, H α, and H β emission lines. The details of the MCRT calculations and insights into the physics of Ly α escape from disc-like galaxies are presented in our companion study (Smith et al. 2021).

In this work, we carefully analyse these detailed numerical radiative transfer simulations to shed more light on the emission, absorption, and scattering of Balmer H α and H β photons. In particular, we focus on answering questions related to the source properties (collisional excitation versus recombination emission), transport or radiation (dust scattering and absorption), importance and origins of the DIG (including extraplanar emission), and the connection between H α and star formation (including SFR time-scales). Furthermore, we are looking forward to future applications of our methodology, including cosmological simulations based on the same framework in conjunction with the THESAN project (Garaldi et al. 2021; Kannan et al. 2022; Smith et al. 2022). This will help improve our understandings of the physics and observational interpretations for star-forming galaxies in the high-redshift Universe.

We introduce the simulations and the performed MCRT calculations in Section 2. We then show in Section 3 that our simulation produces realistic spatial distributions of H α and H β emission by comparing to measurements of local galaxies. The key results concerning the emission, scattering, and absorption of the Balmer emission lines are described in Section 4. We focus on H α as an SFR tracer in Section 5 by discussing the Balmer decrement for performing dust attenuation corrections and the time-scale of the H α SFR indicator. Finally, we discuss limitations and future prospects in Section 6, before concluding in Section 7. Throughout this paper, we employ a Chabrier (2003) initial mass function (IMF). Luminosities, masses, and SFRs are calculated assuming a Planck2015 cosmology (Planck Collaboration XIII 2016).

2 METHODS

We describe in Section 2.1 the simulations, which are based on a novel framework to self-consistently model the effects of radiation fields, dust physics, and molecular chemistry (H_2) in the ISM of galaxies. In particular, we focus on idealized simulations of MW-like and LMC-like galaxies. Section 2.2 gives a brief overview of the MCRT calculations employed in order to predict the H α and H β emission from the aforementioned simulations. Further details on the MCRT methodology and the Ly α emission of those simulations are presented in our companion paper (Smith et al. 2021). To illustrate the typical properties of the isolated MW simulation, Fig. 1 shows projected images of the MW galaxy at 713 Myr for both face-on and edge-on views of the stellar mass surface density, SFR surface density, gas mass surface density, and H α surface brightness.

2.1 Isolated MW and LMC simulations

We use the simulations presented in Kannan et al. (2020) and Kannan et al. (2021b). Specifically, we focus on high-resolution isolated simulations of a Milky-Way-like galaxy (MW; $M_{\mathrm{halo}} = 1.5 \times 10^{12}\ \mathrm{M}_{\odot}$) and an LMC-like galaxy (LMC; $M_{\mathrm{halo}} = 1.1 \times 10^{11}\ \mathrm{M}_{\odot}$). The simulations were performed with AREPO-RT (Kannan et al. 2019), a novel radiation hydrodynamic extension of the moving mesh hydrodynamic code AREPO (Springel 2010; Weinberger, Springel & Pakmor 2020).[1] The adopted sub-grid models for star formation and feedback are described in Marinacci et al. (2019) and Kannan et al. (2020). Briefly, gas is allowed to cool down to 10 K with the cooling function divided into primordial cooling from hydrogen (both molecular and atomic) and helium, metal cooling scaled linearly with the metallicity of the gas and cooling through gas-dust and radiation field interactions, in addition to photoelectric and photoheating from far-ultraviolet (FUV) and Lyman continuum photons, respectively. Star particles are probabilistically formed from cold gas above a

[1]Public code access and documentation available at `arepo-code.org`.

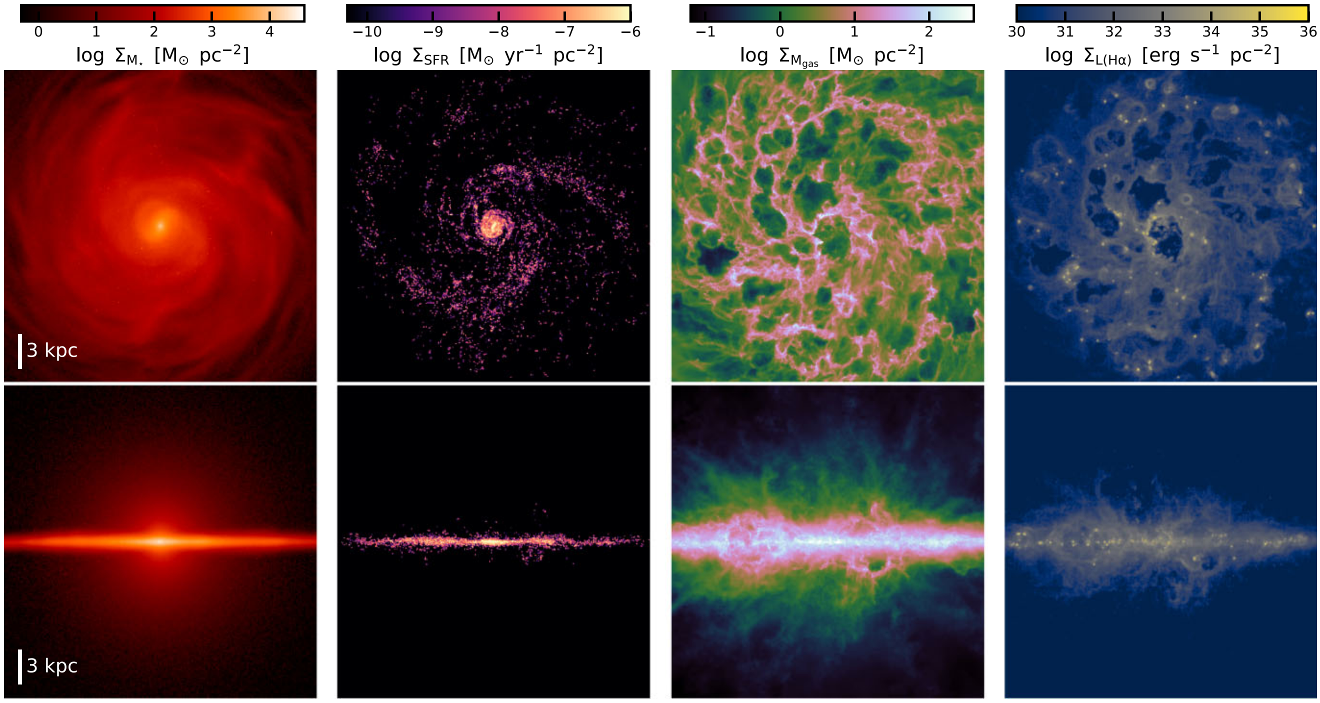

Figure 1. MW simulation at 713 Myr. Maps of stellar mass, SFR (averaged over the past 100 Myr), gas mass, and H α luminosity are shown from left to right. The stellar mass, SFR, and H α are smoothed by 50 pc in order to increase visibility. The top and bottom panels show face-on and edge-on projections, respectively. The dimensions of each map are 30 × 30 kpc (the ruler in the bottom left indicates 3 kpc). The star formation is concentrated at the centre and spiral arms, while the H α emission traces the young, compact H II regions, and supernova bubbles. The corresponding LMC-BC03 maps are shown in Appendix A1.

density threshold of $n = 10^3$ cm^{-3}. Additionally, the star-forming gas cloud needs to be self-gravitating in order to form stars. There are three feedback mechanisms implemented related to stars: radiative feedback, stellar winds from young O, B, and asymptotic giant branch (AGB) stars, and supernova feedback. Photoheating, radiation pressure, and photoelectric heating are modelled self-consistently through the radiative transfer scheme. Furthermore, the simulations employ a novel self-consistent dust formation and destruction model (McKinnon, Torrey & Vogelsberger 2016; McKinnon et al. 2017), which accounts for three distinct dust production channels: SNII, SNIa, and AGB stars (Dwek 1998). The dust is assumed to be dynamically coupled to the gas. The dust mass in the ISM increases due to the gas-phase elements colliding with existing grains (Dwek 1998) and decreases due to shocks from SN remnants (McKee 1989) and sputtering in high-temperature gas (Tsai & Mathews 1995). The resulting dust properties are presented in detail in Kannan et al. (2020). Briefly, the dust-to-gas ratio of the simulations is 0.01–0.014 (the canonical MW value is 0.01), with a weak increase towards the central region in the galaxy, towards higher gas density, and towards lower temperature (their figs 9 and 10).

Important for this work, we assume the Bruzual & Charlot (2003, hereafter BC03) model as our fiducial stellar population synthesis (SPS) model. In order to see how this assumption affects our results, we also run the LMC model with the Binary Population and Spectral Synthesis (BPASS) model (v2.2.1; Eldridge & Stanway 2009; Eldridge et al. 2017).[2] We denote these runs as LMC-BC03 and LMC-BPASS. For all SPS models, we assume a Chabrier (2003) IMF with a high-mass cut-off of 100 M$_\odot$. Importantly, we incorporate the different SPS models fully self-consistently, i.e. we take into account both the change of the production rate of ionizing photons with stellar age (Appendix B) and the strength and timing of radiative feedback, stellar winds, and supernova feedback.

The MW and LMC simulations consist of a dark matter halo, a bulge, and a stellar and gaseous disc set-up following the techniques described in Hernquist (1993) and Springel & Hernquist (2005). The dark matter halo is modelled as a static background gravitational field that is not impacted by the baryonic physics. The full set-up parameters are listed in table 2 of Kannan et al. (2020) but we outline the most relevant details here. The simulation box sizes for the MW and LMC simulations are 600 and 200 kpc, respectively. The dark matter halo and the bulge are modelled as Hernquist profiles (Hernquist 1990). The initial gas and the stellar discs are exponential profiles with effective radii of 6 (2.8) kpc and 3 (1.4) kpc for the MW (LMC) simulation, respectively. The vertical profile of the stellar disc follows a sech^2 functional form with a scale height of 300 (140) pc for the MW (LMC) simulation and initial stellar ages are taken to be 5 Gyr to minimize spurious ionization. The initial gas fractions are 16 (19) per cent for the MW (LMC) and the distributions are computed self-consistently assuming hydrostatic equilibrium. The initial gas temperature is set to 10^4 K and the initial metallicity to 1 Z$_\odot$ (0.5 Z$_\odot$) for the MW (LMC) simulation. The production of new metals is turned off in order to suppress unrealistic gas metallicities, caused by the lack of cosmological gas inflow into the disc. The MW and LMC simulations are run with a stellar mass resolution of 2.8×10^3 M$_\odot$ and a gas mass resolution of 1.4×10^3 M$_\odot$. The corresponding gravitational softening lengths are $\epsilon_\star = 7.1$ pc and $\epsilon_{\rm gas} = 3.6$ pc, respectively. The simulations are each run for 1 Gyr.

After starting the simulations, they settle into equilibrium after about 200 Myr (Kannan et al. 2020). In this paper, we disregard these

[2]See the project website at bpass.auckland.ac.nz.

Table 1. Median properties of the MW, LMC-BC03, and LMC-BPASS simulations. The $M_\star$, $M_{\rm gas}$, and SFR are measured within an aperture of 15 kpc. The SFR_{50} is measured over 50 Myr (stars formed in the past 50 Myr). The effective radius $R_{\rm eff}$ is the half-mass size.

Simulation	$M_{\rm halo}$ (M$_\odot$)	$M_\star$ (M$_\odot$)	$M_{\rm gas}$ (M$_\odot$)	SFR_{50} (M$_\odot$ yr^{-1})	$R_{\rm eff}$ (kpc)
MW	1.5×10^{12}	6.2×10^{10}	4.2×10^{9}	2.7	4.4
LMC-BC03	1.1×10^{11}	3.5×10^{9}	5.2×10^{8}	0.043	2.2
LMC-BPASS	1.1×10^{11}	3.5×10^{9}	5.2×10^{8}	0.041	2.2

first 200 Myr when computing average or median properties across all snapshots if not otherwise stated. The median values of the key properties of the MW, LMC-BC03, and LMC-BPASS simulations are highlighted in Table 1. We find an SFR (averaged over the past 50 Myr) for the MW, LMC-BC03, and LMC-BPASS simulations of 2.7, 0.043, and 0.041 M$_\odot$ yr^{-1}, respectively. As we will show below, although these stellar and gas properties for the LMC-BC03 and LMC-BPASS model are basically indistinguishable, the Balmer emission from these two models are quite distinct.

2.2 Radiative transfer of Balmer emission lines

We give a schematic overview of the H α radiative transfer in Fig. 2. We employ the Cosmic Ly α Transfer code (COLT; Smith et al. 2015, 2019)[3] to perform post-processing MCRT calculations, briefly summarizing the most relevant details here. In particular, the dominant source of H α photons is via cascade recombination of recently ionized hydrogen atoms, with a small contribution of collisional excitation emission. To ensure accurate photon conserving ionization states for line radiative transfer we performed post-processing photoionization equilibrium calculations with COLT, which was implemented as an MCRT module mirroring the physics of galaxy formation simulations (Rosdahl et al. 2013; Kannan et al. 2019). This is also helpful as the simulations do not fully resolve the temperature and density substructure of a fraction of the young H II regions where line emission is especially strong (see the discussion in our companion paper; Smith et al. 2021). We retain the gas temperature as this is already faithfully modelled but we iteratively recalculate the ionizing radiation field in three bands (H I, He I, and He II) and update the ionization states assuming ionization equilibrium stopping this process when the global recombination emission is converged to within a 0.1 per cent relative difference. The solver also includes dust absorption and anisotropic scattering, collisional ionization, and a meta-galactic UV background with self-shielding (Faucher-Giguère et al. 2009; Rahmati et al. 2013). We employ 10^8 photon packets in the MCRT calculations, which is adequate to represent the ionizing radiation field based on sampling from the age and metallicity-dependent stellar SEDs in terms of position, direction, and frequency. The COLT output images capture the photon properties at a pixel resolution of 10 pc oriented in face-on and edge-on directions. This resolution was chosen as a compromise to be higher than observations while also not requiring too much data (already 6000^2 pixels) or degrading the MCRT signal-to-noise ratio.

For the line radiative transfer we calculate the resolved H α and H β luminosity caused by radiative recombination as

$$L_X^{\rm rec} = h\nu_X \int P_{{\rm B},X}(T, n_e)\alpha_{\rm B}(T)\, n_e n_p \,{\rm d}V, \quad (1)$$

[3]For public code access and documentation see `colt.readthedocs.io`.

where $X \in \{{\rm H}\alpha, {\rm H}\beta\}$ denotes the line, $h\nu_X = \{1.89, 2.55\}$ eV is the energy at line centre, $P_{\rm B}$ is the conversion probability per recombination event (e.g. $P_{{\rm B},X}(10^4\,{\rm K}) \approx \{0.45, 0.12\}$), $\alpha_{\rm B}$ is the case B recombination coefficient, and the number densities n_e and n_p are for free electrons and protons, respectively. We also calculate the resolved radiative de-excitation of collisional excitation of neutral hydrogen by free electrons as

$$L_X^{\rm col} = h\nu_X \int q_{{\rm col},X}(T)\, n_e n_{\rm H\,I}\,{\rm d}V, \quad (2)$$

where $q_{{\rm col},X}$ is the collisional rate coefficient and $n_{\rm H\,I}$ is the number density of neutral hydrogen.

Stellar continuum spectral luminosities $L_{\lambda,\,{\rm cont}}$ for each line are tabulated by age and metallicity based on the SEDs around the reference wavelengths, which is included to enable self-consistent predictions for line equivalent width (EW) measurements. We emphasize that, since the metal enrichment is ignored, all stars have equal metallicity: 1.0 $Z_\odot$ and 0.5 $Z_\odot$ in the MW and the LMC case, respectively. The dust distribution is also self-consistently taken from the simulation such that the local dust absorption coefficient is

$$k_{{\rm d},X} = \kappa_{{\rm d},X}\mathcal{D}\rho, \quad (3)$$

where the dust opacity is $\kappa_{{\rm d},X} = \{6627, 10\,220\}$ cm^2 g^{-1} of dust and the dust-to-gas ratio is $\mathcal{D}$. Dust scattering is modelled based on the albedo $A = \{0.6741, 0.6650\}$ and anisotropic Henyey–Greenstein phase function with asymmetry parameter of $\langle\cos\theta\rangle = \{0.4967, 0.5561\}$, all of which are based on the fiducial Milky Way dust model from Weingartner & Draine (2001). With the 10^8 photon packets in the line MCRT calculations, we are able to capture the escaping photon properties and high signal-to-noise images oriented in face-on and edge-on directions. For each of these lines and cameras we also calculate ray-tracing-based images of the intrinsic and dust-attenuated line emission based on the adaptive convergence algorithm described in appendix A of Yang et al. (2020). This method eliminates Monte Carlo noise at the expense of treating dust as purely absorbing; i.e. assuming an albedo of $A = 0$.

3 COMPARISON TO OBSERVATIONS

Before discussing the physics of the predicted H α and H β emission from our simulation, we show in this section that the predicted surface brightness profiles are consistent with observations of MW- and LMC-like galaxies in the local Universe. In particular, we compare the radial H α and H β emission line profiles to observational measurements of the SDSS/MaNGA survey in Section 3.1, while Section 3.2 compares the vertical scale heights.

3.1 Radial profiles from SDSS/MaNGA

We compare our simulated H α maps to SDSS/MaNGA observations (Bundy et al. 2015). Specifically, we aim at comparing the shapes of the H α and H β surface brightness profiles. MaNGA provides high-quality optical (3600–10 300 Å and a spectral resolution of $R \sim 2000$) integral field unit (IFU) spectroscopy for a large ($\sim$ 10 000) sample of low-redshift galaxies. Individual galaxies are covered out to a distance of 1.5–2.5 effective radii.

We use DR-15 (Aguado et al. 2019), which provides the data reduced by the Data Reduction Pipeline (DRP; Law et al. 2016) and stellar and gas properties of the galaxies made available due to the Data Analysis Pipeline (DAP; Belfiore et al. 2019; Westfall et al. 2019). We accessed, inspected, and downloaded the data cubes with `Marvin` (Cherinka et al. 2019). The H α and H β emission line maps

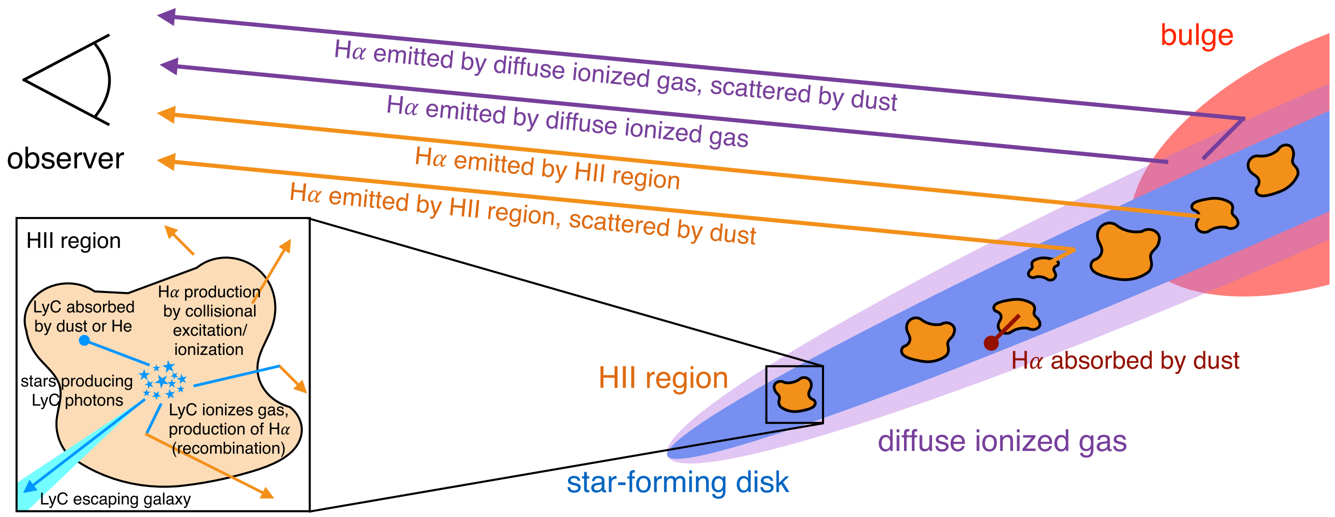

Figure 2. Schema of the H α radiative transfer. H α that reaches the observer can either be emitted by nebular H II regions or DIG. In this study, we differentiate between H II regions and the DIG with a simple gas density cut at $n_{\rm thresh} = 100\ {\rm cm}^{-3}$, though we also investigate other definitions and their implications (Section 4.5). H α photons are produced by collisional excitation, by collisional ionization, and by recombination of ionized gas, which is ionized by Lyman continuum (LyC) photons. Both LyC and H α photons can also be scattered or absorbed by dust. Furthermore, some LyC photons are consumed by He, leading to the photoionization of He I and He II. In the case of the MW simulation, on average ~ 28 per cent of the LyC photons are absorbed by dust, ~ 8 per cent ionize He I, ~ 1 per cent ionize He II, ~ 6 per cent escape the galaxy, implying that only about $f_{\rm H} \approx 57$ per cent of the produced LyC photons are available for ionizing hydrogen and the production of H α (Section 5.2).

have been corrected for stellar absorption and Milky Way reddening using the O'Donnell (1994) reddening law.

For both the MW and LMC simulations, we construct a sample of galaxies from MaNGA. Our selection is based on both stellar mass and SFR. We use as a rough estimate of the SFR the H α-based SFR within the IFU field of view provided by DAP. For the stellar mass, we use the NASA Sloan Atlas (NSA; Blanton et al. 2005, 2011) catalogue, which provides stellar masses derived from elliptical Petrosian photometry. Specifically, for the MW comparison sample, we select galaxies with stellar masses of $\log(M_\star/{\rm M}_\odot) = 10.6$–$10.9$ and ${\rm SFR}/({\rm M}_\odot\ {\rm yr}^{-1}) = 0.5$–$5.0$, which is consistent with $M_\star$ and SFR from our MW simulation (Table 1). For the LMC comparison sample, we select galaxies with stellar masses of $\log(M_\star/{\rm M}_\odot) = 9.4$–$9.6$ and ${\rm SFR}/({\rm M}_\odot\ {\rm yr}^{-1}) = 0.01$–$0.1$. In both comparison samples, we exclude any galaxies with DAP datacube quality flags cautioning 'do not use', with two or more 'warning' flags, as well as objects that are irregular (visual inspection of the H α maps). This yields MW and LMC comparison samples of 52 and 59 galaxies, respectively.

For each MaNGA galaxy, we measure the H α and H β surface brightness profiles in the same elliptical apertures in order to account for the effect of inclination on radius measurements. Furthermore, we only consider spaxels with a signal-to-noise ratio of at least 5. Since we aim for a comparison of the shapes, we normalize each individual profile to a total luminosity of 10^{42} erg s^{-1} (10^{41} erg s^{-1}) for the case of H α (H β). We then compute the median profile and 1σ variation as a function of radius. We have also experimented with masking regions of active galactic nuclei (AGNs) – and other excitation mechanisms – via BPT diagnostics (Baldwin, Phillips & Terlevich 1981), finding this had a negligible effect on our median-stacked profile (reduction of 0.2 dex in the centre relative to the outskirts).

In order to compare the observed median H α and H β profiles to our simulated ones, we need to account for the point spread function (PSF). MaNGA has a relatively large PSF with a full width at half-maximum (FWHM) of 2.5 arcsec (Bundy et al. 2015). This corresponds to an angular distance of 3.9 and 1.7 kpc at the average distance of our MW sample ($\langle z\rangle = 0.078$) and LMC sample ($\langle z\rangle = 0.036$), respectively. We apply a Gaussian PSF to the simulated H α and H β face-on maps (see Appendix A2) and then measure the profiles in circular apertures. We compute the median H α and H β profiles (again after normalizing each profile) of all snapshots after 200 Myr, which ensures that the simulations have reached a quasi-steady state (see Section 2.1).

In Fig. 3, we compare our simulated H α and H β profiles (solid lines; dotted in case for the LMC-BPASS simulation) with the observed MaNGA profiles (points with errorbars). We find excellent agreement in the overall shapes for both the MW simulation out to 10–15 kpc (left-hand panel) and LMC simulations out to 4–6 kpc (right-hand panel). To guide the eye, the green dashed lines show a Sérsic $n = 1$ profile, indicating that both the simulated and observed profiles are well described by an exponential function in the case of the MW, while the profiles appear to be steeper in the case of the LMC. An important note is that nuclear regions are not modelled in the simulation and effects due to AGN feedback are not included (see e.g. Nelson et al. 2021), so we do not expect or judge the agreement there as the consistency could be serendipitous. Furthermore, we find little difference between the surface brightness profile of the LMC-BC03 and the LMC-BPASS model.

3.2 Vertical scale heights

The comparison of the vertical profiles from simulations with observations is more challenging than the aforementioned comparison of the radial profiles. The main reason for this is the lack of observational data probing H α of edge-on MW-like galaxies. A recent investigation by Jo et al. (2018) measured the vertical profiles of the extraplanar H α emission for 38 nearby edge-on late-type galaxies. The data have been taken from six different H α imaging surveys. The galaxies were selected to be within a distance of 30 Mpc, have no noticeable spiral or asymmetry patterns, and only include data of sufficient quality (based on signal-to-noise ratios). The resulting 38 galaxies span a wide range in SFRs (${\rm SFR} = 0.001$–$1.5\ {\rm M}_\odot\ {\rm yr}^{-1}$), so we sub-select

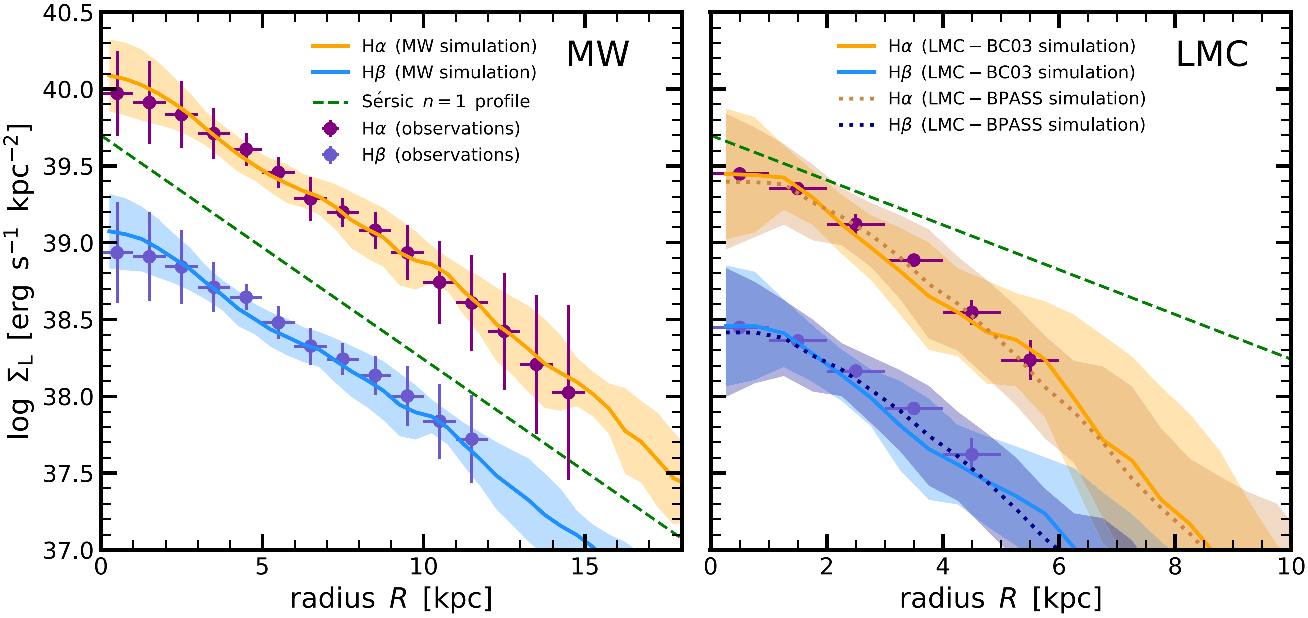

Figure 3. Comparison of the predicted H α and H β surface brightness profiles from the simulations with the observed ones from the MaNGA survey. The left-hand panel shows the MW simulation run: The solid lines show the median of the simulations, while the points with errorbars mark the observational measurements. The right-hand panel shows the results for the LMC-BC03 (solid lines) and LMC-BPASS (dotted lines) simulations. The shaded regions and the errorbars show the 16–84th percentiles. The H α (H β) profiles have been normalized to a total luminosity of 10^{42} erg s^{-1} (10^{41} erg s^{-1}). In both panels, the green dashed line shows an arbitrarily normalized Sérsic profile with Sérsic index $n = 1$, indicating that the H α and H β profiles are roughly exponential in both observations and simulations. In both the MW and LMC case, the simulations are able to reproduce the observed profiles out to 10–15 kpc.

from this observational sample galaxies with SFR > 0.1 M$_{\odot}$ yr^{-1} that also show disturbed discs. These criteria lead to a sample size of 12 galaxies for the MW comparison. We do not perform a comparison with the LMC simulations because of a lack of matching comparison sample of galaxies. For each galaxy, Jo et al. (2018) obtained the vertical profiles of the H α emission by horizontally averaging each image and then fitting the profiles with an exponential function ($\propto \exp(-z/Z_{\mathrm{H}\alpha})$), where $Z_{\mathrm{H}\alpha}$ is the scale height.

We estimate the scale height $Z_{\mathrm{H}\alpha}$ in the simulations adopting the same procedure as the observations. Specifically, we compute the H α vertical profiles for each snapshot by horizontally averaging the edge-on projection within the effective radius ($R_{\mathrm{eff}} = 4.3$ kpc) and then fitting an exponential function to estimate $Z_{\mathrm{H}\alpha}$. We consider only the snapshots 200 Myr after the start of the simulation. In order to compare our $Z_{\mathrm{H}\alpha}$ from the simulation with observations, we also add a relative uncertainty of 30 per cent.

The right-hand panel of Fig. 4 shows the scale height distributions of the observations by Jo et al. (2018) in black. The median observed scale height is $0.7^{+0.3}_{-0.1}$ kpc. The scale height distribution for our simulation is shown in red (with observational uncertainty) and in orange (without observational uncertainty). We measure a median scale height in the simulation of $0.7^{+0.4}_{-0.2}$ kpc, demonstrating that the scale heights from the MW simulation are overall in good agreement with the observations. For reference, the scale height for the stellar mass ($Z_{\star} = 0.26$ kpc), dust mass ($Z_{\mathrm{dust}} = 0.23$ kpc), and gas mass ($Z_{\mathrm{gas}} = 0.56$ kpc) and SFR ($Z_{\mathrm{SFR}} = 0.12$ kpc) are indicated as vertical arrows. This already hints at *in situ* ionization of gas, rather than H α photons scattered on dust into the observer's line of sight, being the main driver of this extraplanar H α emission. We will look further into this in Section 4.6. For completeness, the left-hand panels of Fig. 4 show the equivalent plot and numbers for the LMC-BC03 (top) and LMC-BPASS (bottom) simulations. We find that the LMC simulations have comparable scale heights for the gas and H α (independent of the stellar population model) to the MW simulation, while the SFR and stellar mass scale heights of the LMC are smaller than the ones of the MW. We attribute the relatively large gas and H α scale heights of the LMC to the more variable star formation in the LMC than the MW simulation.

4 BALMER EMISSION, SCATTERING, AND ABSORPTION

After showing in the previous section that the Balmer (H α and H β) emission of our MW and LMC simulations are realistic, we now turn towards understanding the Balmer emission, scattering, and absorption. Specifically, we present results on the gas temperature and density dependence of the Balmer emission (Section 4.1), the collisional excitation, and recombination emission (Section 4.2), the importance of scattering (Section 4.3), the radiative transfer of photons from H II and DIG regions (Section 4.4), different DIG definitions (Section 4.5), and the origin of the extraplanar Balmer emission (Section 4.6).

4.1 Density–temperature dependence of the Balmer emission

In Fig. 5, we show the density and temperature dependence of the Balmer line emission. We have adopted this figure from our companion work (Smith et al. 2021), which goes into further detail regarding the gas that emits Ly α and Balmer emission. Here, we plot the density–temperature phase space diagram colour-coded by the relative intrinsic H α luminosity, the relative observed H α luminosity, and the escape fraction of H α (ratio of observed and intrinsic emission). In all panels, the contours indicate the mass-weighted distribution of the gas, while the vertical lines show the

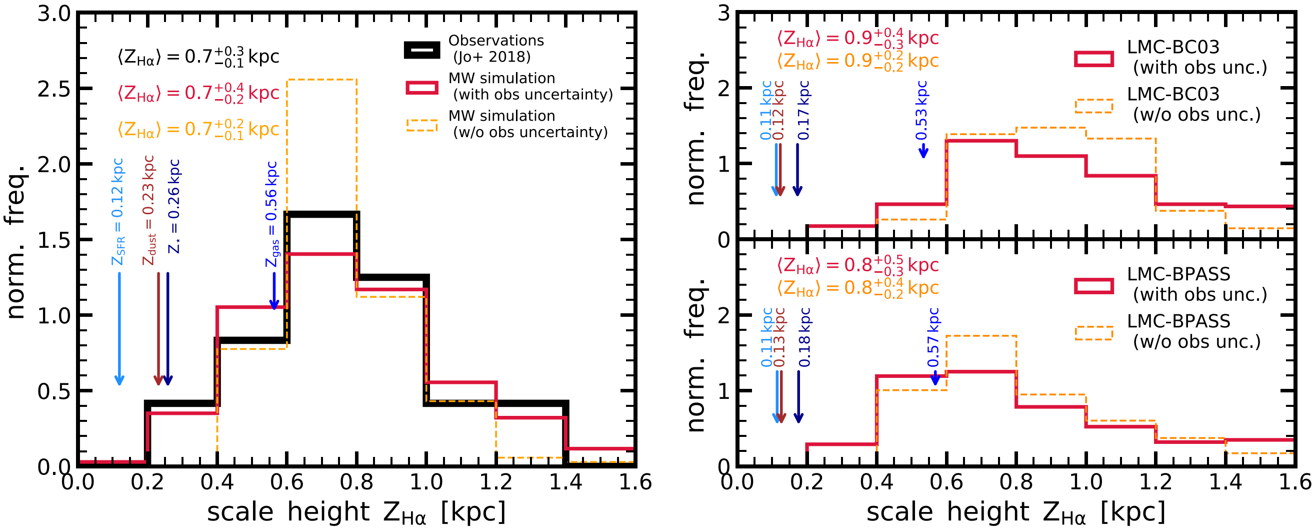

Figure 4. Comparison of the vertical H α scale heights $Z_{H\alpha}$ of the simulations with observations. The left-hand panel shows the MW simulation, while the right two panels show the LMC-BC03 (top) and the LMC-BPASS (bottom) simulations. For the LMC, no observational data for a comparison are available. The scale heights in both observations and simulations are measured by fitting an exponential function ($\propto \exp(-z/Z_{H\alpha})$) to the vertical profiles of the H α emission. The observations are taken from scale height measurements by Jo et al. (2018) of 12 nearby edge-one late-type galaxies. For the MW simulation, we find a typical scale height of $Z_{H\alpha} = 0.7$ kpc in both observations and simulations. After accounting for the observational uncertainty, also the overall distribution are in good agreement with each other. For reference, the MW scale height for the stellar mass ($Z_{\star} = 0.26$ kpc), dust mass ($Z_{\rm dust} = 0.23$ kpc), and gas mass ($Z_{\rm gas} = 0.56$ kpc) and SFR ($Z_{\rm SFR} = 0.12$ kpc) are indicated. For the LMC, we find the scale heights of H α, the SFR, and the gas to be comparable to the ones of the MW, while the the scale heights for the stellar mass and dust mass tend to be smaller.

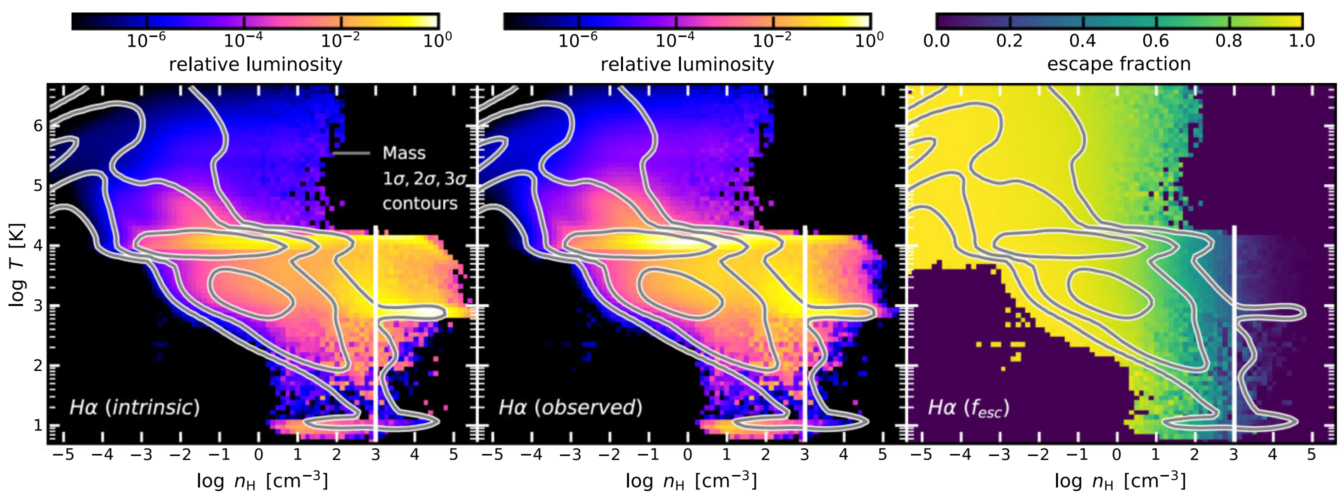

Figure 5. Density and temperature dependence of the Balmer H α line emission across all snapshots of the MW simulation. From left to right, we plot the density–temperature phase space diagram colour-coded by the relative intrinsic H α luminosity, the relative observed H α luminosity, and the escape fraction of H α (ratio of observed and intrinsic emission). The contours indicate the mass-weighted distribution of the gas, while the vertical lines show the star-formation threshold. Most of the intrinsic H α emission comes from dense H II regions with a characteristic temperature of $T \sim 10^3$–10^4 K, while the observed H α emission stems from $T \sim 10^4$ K gas. The impact of dust absorption can also be seen: the denser the gas, the more pronounced the dust absorption and hence the lower the escape fraction.

star-formation threshold. The mass contours highlight the presence of molecular gas (~ 10 K) and of collapsing structures prior to heating and disruption via feedback ($\sim 10^3$ K). Importantly, although density is the only direct star-formation condition, the temperature enters indirectly through Jeans stability and converging flows (see Marinacci et al. 2019 and Kannan et al. 2020 for more details). This ensures that stars only form within cold ($\sim$10 K) molecular clouds and the warm $\sim$10^3 K track is high-density photoheated gas surrounding young stars that has not had time to become a lower density 10^4 K H II region.

We find that most of the observed H α emission comes from dense H II regions with a characteristic temperature of $T \sim 10^4$ K and density of $n_{\rm H} \sim 0.1$–$10\,{\rm cm}^{-3}$ (middle panel of Fig. 5). The intrinsic H α emission (left-hand panel of Fig. 5) also shows strong emission features at $T \sim 10^3$ K, which are caused by both physical and numerical effects. On the numerical side, this feature can be associated with

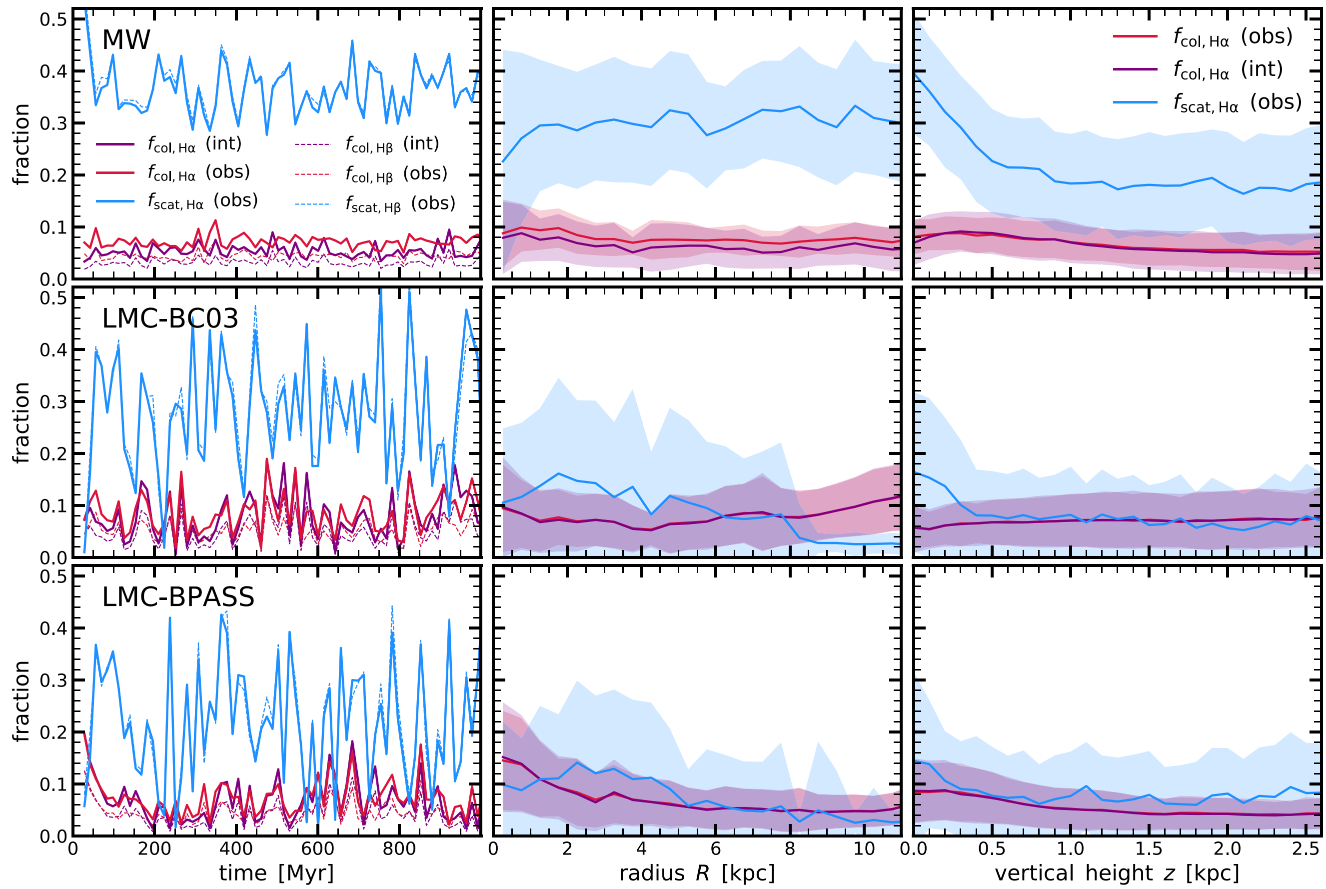

Figure 6. Importance of collisional excitation emission ($f_{\rm col}$) and scattered emission ($f_{\rm scat}$). The panel on the left, middle, and right show the time-evolving global value, azimuthally averaged radial profile, and vertical profile, respectively. The MW, LMC-BC03, and LMC-BPASS simulations are shown from top to bottom, with the LMC simulations showing more variability with time. The solid (dashed) red and purple lines show $f_{\rm col}$ for the intrinsic and observed H α (H β) emission, respectively. The corresponding blue lines show the fractional increase of observed emission caused by scattering (i.e. $f_{\rm scat} = 1 - L_{\rm w/o\ scattering}/L_{\rm with\ scattering}$). We find median values of $f_{\rm col} = 5.0^{+1.7}_{-0.8}$ per cent ($f_{\rm col} = 6.7^{+6.1}_{-3.7}$ per cent and $f_{\rm col} = 6.0^{+4.5}_{-3.2}$ per cent) and $f_{\rm col} = 7.1^{+0.9}_{-1.0}$ per cent ($f_{\rm col} = 8.2^{+3.1}_{-3.9}$ per cent and $f_{\rm col} = 7.1^{+2.8}_{-3.3}$ per cent) for the intrinsic and observed H α emission for the MW (LMC-BC03 and LMC-BPASS) simulation, respectively, indicating that the Balmer H α and H β emission is dominated by radiative recombination as opposed to collisional excitation. Furthermore, scattering is important ($f_{\rm scat} = 37^{+4}_{-5}$ per cent for the MW, $f_{\rm scat} = 28^{+11}_{-11}$ per cent for the LMC-BC03, and $f_{\rm scat} = 21^{+14}_{-12}$ per cent for the LMC-BPASS) in boosting the Balmer emission by allowing Balmer photons to scatter out of dust-obscured regions both in the face-on and edge-on directions. There are only weak radial gradients in both $f_{\rm col}$ and $f_{\rm scat}$ (middle panels), while the $f_{\rm scat}$ and $f_{\rm col}$ decrease with increasing scale height (right-hand panels).

underresolved and consequently underheated H II regions (see also Smith et al. 2021 for an extended discussion of this). On the physical side, as noted above, this feature can be caused by molecular clouds, partial ionization, and transient phenomena. Importantly, although the intrinsic H α emission is bimodal, this second peak at high densities and temperatures of $T \sim 10^3$ K diminishes when looking at the observed H α emission (i.e. after scattering and absorption), because the escape fractions from these same dense dusty regions are much lower in comparison to resolved H II regions at $\sim 10^4$ K. This can be clearly seen in the right-hand panel of Fig. 5, which shows the H α escape fraction strongly scales with the density of gas.

4.2 Emission: collisional excitation and recombination

As shown in the schema of the H α radiative transfer (Fig. 2), recombination, collisional excitation, and collisional ionization can lead to Balmer emission. In this section, we focus on the importance of collisional excitation emission since the emission from collisional ionization contributes less than 2 per cent to the total H α emission. In Fig. 6, we show the fraction of collisional excitation emission $f_{\rm col}$ for the MW (top panels), LMC-BC03 (middle panels), and LMC-BPASS (bottom panels) simulations. We plot the integrated $f_{\rm col}$ as a function of time, the average $f_{\rm col}$ as a function of radial distance, and the average $f_{\rm col}$ as a function of vertical scale height in the left-, middle, and right-hand panels, respectively. The solid (dashed) purple and red lines show $f_{\rm col}$ for the intrinsic and observed H α (H β) emission.

The observed emission typically has a higher $f_{\rm col}$ than the intrinsic emission, since collisional excitation emission is emitted in regions with lower density and therefore suffers less dust absorption. For the MW, we find a median value of $f_{\rm col} = 5.0^{+1.7}_{-0.8}$ per cent and $f_{\rm col} = 7.1^{+0.9}_{-1.0}$ per cent for the intrinsic and observed H α emission, respectively. For the LMC-BC03, we find $f_{\rm col} = 6.7^{+6.1}_{-3.7}$ per cent and $f_{\rm col} = 8.2^{+3.1}_{-3.9}$ per cent for the intrinsic and observed H α emission, while the LMC-BPASS returns $f_{\rm col} = 6.0^{+4.5}_{-3.2}$ per cent and $f_{\rm col} = 7.1^{+2.8}_{-3.3}$ per cent, indicating that changes to the stellar population models lead to small changes in $f_{\rm col}$. These slightly larger values for the intrinsic and observed $f_{\rm col}$ can be explained by the more turbulent and bursty nature of the LMC relative to the MW, which gives rise to more shocks and therefore collisionally excited gas. The variability of $f_{\rm col}$ occurs with the same cadence as star formation fluctuations (see Section 5.1), which is due to a combined effect of having a higher recombination rate during a starburst and higher collisional emission due to feedback. This is also confirmed by the rather large variability of $f_{\rm col}$ in the case of the LMC (the confidence intervals quoted above indicate the 16th and 84th percentiles).

For the H β emission, we find the same overall trends as for H α. We obtain lower $f_{\rm col}$ values than for the H α emission. This can be explained by the lower collisional rate coefficients of H β compared to H α (see appendix A of Smith et al. 2021).

The middle and right-hand panels of Fig. 6 show the median radial and vertical profiles of $f_{\rm col}$. Overall, we do not find a strong gradient in $f_{\rm col}$. If anything, there is a weak trend for the MW where $f_{\rm col}$ is slightly higher in the centre than the outskirts and within the disc rather than above the mid-plane.

In summary, we find that only a small fraction (5–10 per cent) of the total Balmer emission stems from collisionally excited gas. Most of the emission stems from radiative recombination. This is consistent with previous theoretical findings by Peters et al. (2017), who investigated a small region of a galactic disc with solar neighbourhood-like properties in the stratified disc approximation. They found that collisional excitation emission makes up 1–10 per cent of the total Balmer emission.

4.3 Scattering of Hα photons

Fig. 6 also allows us to investigate the importance of scattering of the Balmer emission. In all of the panels, the solid (dashed) blue lines show the fractional increase of observed H α (H β) emission caused by scattering, $f_{\rm scat} \equiv 1 - L_{\rm w/o\ scattering}/L_{\rm with\ scattering}$. There is essentially no difference between H α and H β. We find scattering to be important with, on average, $f_{\rm scat} = 37^{+4}_{-5}$ per cent for the MW, $f_{\rm scat} = 28^{+11}_{-11}$ per cent for the LMC-BC03, and $f_{\rm scat} = 21^{+14}_{-12}$ per cent for the LMC-BPASS. Furthermore, $f_{\rm scat}$ also does not depend significantly on the viewing angle, i.e. face-on versus edge-on projections lead to differences of less than 1–2 per cent. This means that if scattering is *not* considered, one would underestimate the luminosity by 20–40 per cent. The reason for this is that scattering allows Balmer photons to diffuse out of dust-obscured regions. Although the azimuthally averaged radial gradients are weak (middle panels of Fig. 6), we find in the next section that scattering is particularly prominent around H II regions. We find that scattering is high at low scale heights, i.e. within the disc, and then gradually decreases towards larger vertical heights (right-hand panels of Fig. 6).

We investigate in detail the probability that H α photons scatter at least N times in fig. 22 of our companion paper (Smith et al. 2021). Averaged over all photon trajectories from all snapshots and sightlines, we find that 76 per cent (39 per cent) of all H α photons scatter at least once (at least 10 times) for the MW simulation. When only considering the observed (i.e. escaped) H α photons, these fractions reduce to 36 per cent and 0.3 per cent. On average, an intrinsic and observed H α photon scatters 11.7 and 0.8 times, respectively.

4.4 Hα photons originating from H II regions and the DIG

H α can be emitted from H II and DIG regions. Observationally as well as theoretically, there are no clear definitions of what is meant by DIG and various works adopt different definitions. In this work, we use a threshold in gas density to differentiate between H II and the DIG. Specifically, we adopt a gas density threshold of $n_{\rm thresh} = 100\ {\rm cm}^{-3}$. Balmer photons emitted above this threshold are called H II photons, while photons emitted from gas below $n_{\rm thresh}$ are called DIG photons. Although the choice of $n_{\rm thresh}$ is rather arbitrary, it is motivated by being an order-of-magnitude below the density threshold for star formation, which is $n = 10^3\ {\rm cm}^{-3}$ in our simulations (Section 2.1). Looking at the density–temperature phase diagram (Fig. 5), the DIG is dominated by emission from gas with a temperature of roughly $T \sim 10^4$ K. We compare different DIG definitions in Section 4.5.

In Fig. 7, we illustrate the distribution of the H α emission, split into H II and DIG photons for the same MW snapshot as shown in Fig. 1. The upper and lower panels plot the face-on and edge-on views, respectively. The intrinsic H II photons, observed H II photons, intrinsic DIG photons, and observed DIG photons are shown from left to right. The intrinsic H II photons are emitted from very localized regions, which extend only a few tens of pc. The observed H II photons are significantly more extended than the intrinsic H II photons, which can be explained by scattering (see below). The intrinsic and observed DIG photons have similar distributions and are both more extended than the intrinsic and observed H II photon distributions. This is expected, since the DIG photons are emitted from less dense gas that is spatially more extended and the dust reprocessing is minimal. Furthermore, there are several ring-like features in the DIG map, which are shell overdensities created by supernovae bubbles.

Fig. 8 follows the same layout as Fig. 7, but shows from left to right maps of the total observed H α emission, fraction of DIG photons ($f_{\rm DIG}$), scattering factor ($f_{\rm scat}$), and fraction of photons emitted from collisionally excited gas ($f_{\rm col}$). The map of the observed H α emission clearly shows the point-like sources, which are the H II regions. Consistent with Fig. 7, the $f_{\rm DIG}$ map (second from the left) indicates small localized regions with low $f_{\rm DIG}$, which are the H II regions. The rest is dominated by the DIG, including the regions above the plane of the disc.

The second panel from the right in Fig. 8 shows the fractional increase of observed H α emission caused by scattering (see Section 4.3). Comparing it with $f_{\rm DIG}$, we find that the $f_{\rm scat}$ is high where $f_{\rm DIG}$ is low. This highlights that scattering boosts the H α luminosity more significantly in H II regions than in DIG regions. Specifically, averaged over all MW snapshots, the H II luminosity is boosted by $f_{\rm scat,HII} = 64^{+2}_{-2}$ per cent, while DIG luminosity only increases by $f_{\rm scat,DIG} = 18^{+2}_{-2}$ per cent. For comparison, the total boost-factor due to scattering is $f_{\rm scat} = 38^{+4}_{-5}$ per cent (see also Fig. 6). This trend is even more apparent when looking at the LMC simulations, where we find $f_{\rm scat,HII} = 51^{+10}_{-9}$ per cent ($f_{\rm scat,HII} = 52^{+6}_{-13}$ per cent) and $f_{\rm scat,DIG} = 5^{+3}_{-1}$ per cent ($f_{\rm scat,DIG} = 5^{+4}_{-2}$ per cent) for the LMC-BC03 (LMC-BPASS) model.

The panel on the right of Fig. 8 shows the map of the fraction of photons from collisionally excited gas. There are only a few localized regions with $f_{\rm col}$, which are typically at the boundary to low surface brightness regions. It seems $f_{\rm col}$ is more determined by the overall large scale motion of the gas; i.e. regions with elevated or reduced $f_{\rm col}$ are typically a few kpc in size.

4.5 Implications of different DIG definitions

As mentioned in the previous section, our fiducial identification of the DIG is based on a density cut of the emitting gas: DIG photons are emitted by gas with a density of $n < 100\ {\rm cm}^{-3}$. We now explore an additional DIG identification method, which is based on finding clumps in images. Specifically, high surface brightness

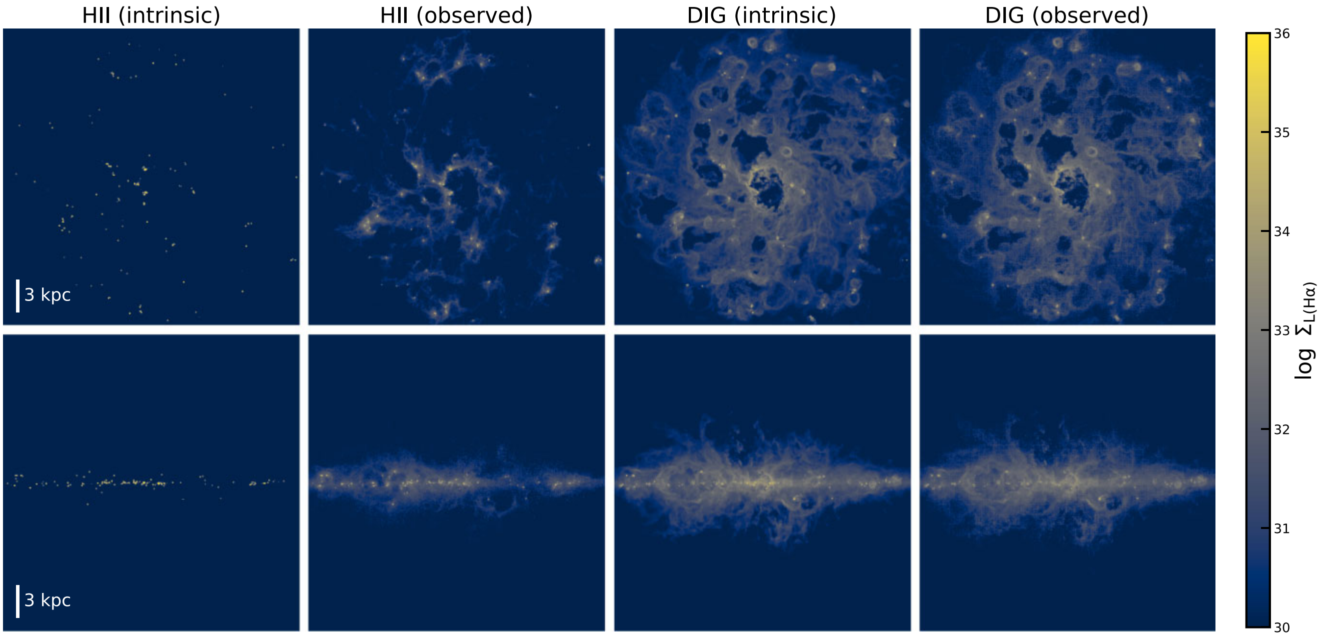

Figure 7. H α emission maps for face-on (upper panels) and edge-on (lower panels) sightlines with dimensions of 30 × 30 kpc. The photons are categorized according to the gas density of the emission region: H II photons (emitted in regions with $n > 100$ cm^{-3}) are shown in the left-hand panels and DIG photons (emitted in regions with $n < 100$ cm^{-3}) are shown in the right-hand panels. For both H II and DIG photons we show the intrinsically emitted photons and the observed (after attenuation and scattering) photons. The H II photons are produced on small, confined regions, and only through scattering are able to occupy a significant area. On the other hand, the DIG photons are emitted on diffuse scales, extending significantly (>3 kpc) above the plane of the disc.

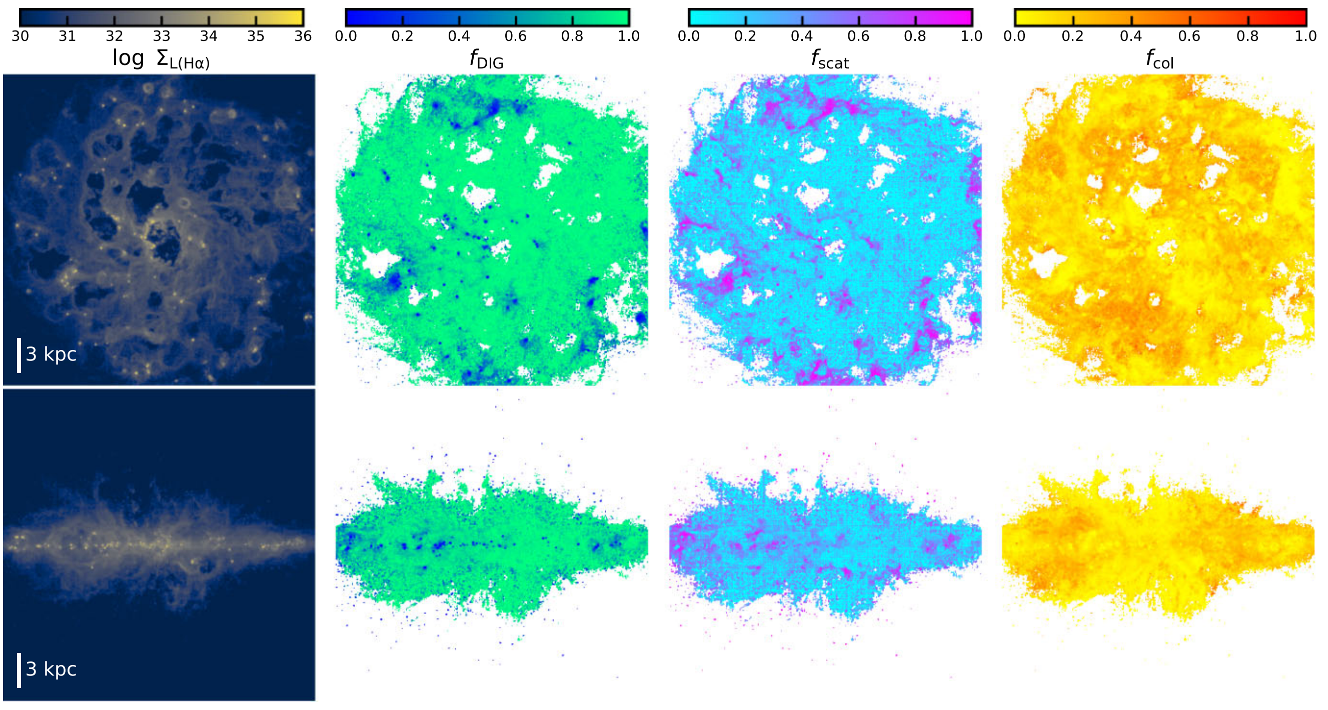

Figure 8. Maps of the observed H α emission (left-hand panels), the fraction of DIG photons (second from the left), the scattering factor (second from the right; $f_{\rm scat} \equiv 1 - L_{\rm w/o\ scattering}/L_{\rm with\ scattering}$), and the fraction of collisionally excited emission (right-hand panels) for face-on (top panels) and edge-on (bottom panels) views. The scattering factor quantifies the fractional increase of observed H α emission caused by scattering. We find that the small-scale, bright regions are dominated by H II photons, while most of the area is dominated by DIG photons. Scattering can boost the luminosity by a factor of $\gtrsim$3 in the bright H II regions.

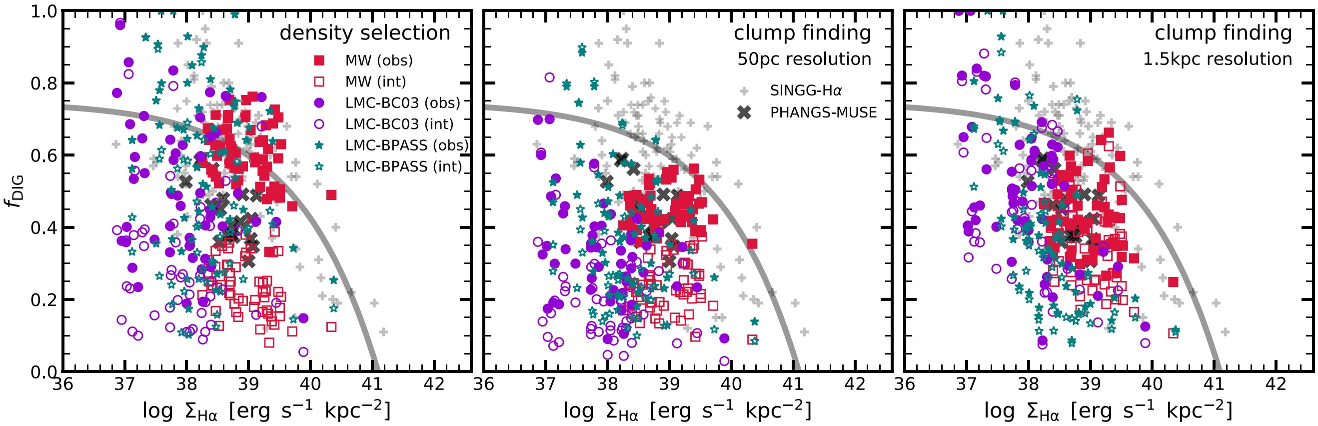

Figure 9. Fraction of Balmer emission originating from DIG $f_{\rm DIG}$ as a function of the H α surface brightness $\Sigma_{\rm H\alpha}$ (equation 4) for different DIG selection methods. The left-hand panel shows our fiducial physical DIG definition that is based on a density cut of the emitting gas, while the middle and right-hand panels use a DIG definition based clump finding on the 2D face-on projection. In all panels, the red squares, purple circles, and teal stars mark our MW, LMC-BC03, and LMC-BPASS simulations, while the filled and empty symbols indicate the observed and intrinsic $f_{\rm DIG}$, respectively. The grey plus and cross symbols are the observational measurements from the SINGG H α survey (Oey et al. 2007; with a median of $f_{\rm DIG} = 0.66^{+0.13}_{-0.12}$ in the MW's $\Sigma_{\rm H\alpha}$ range) and the PHANGS-MUSE survey (Belfiore et al. 2022; with a median of $f_{\rm DIG} = 0.42^{+0.11}_{-0.05}$). The grey solid line shows the best-fitting function (equation 5; Sanders et al. 2017) of the form $f_{\rm DIG} \propto \Sigma_{\rm H\alpha}^{1/3}$, as suggested by Oey et al. on theoretical arguments. The following are the two key conclusions from this figure: (i) $f_{\rm DIG}$ values depend significantly on the selection technique; (ii) $f_{\rm DIG}$ from the clump finding method depends heavily on the spatial resolution of the data; and (iii) the intrinsic $f_{\rm DIG}$ is typically smaller (factor of 2–3) than the observed $f_{\rm DIG}$ due to the comparatively higher escape fractions.

regions (clumps) are classified as H II regions, while the remaining diffuse emission is classified as DIG. This is similar to what is done in some observational data (e.g. Thilker, Braun & Walterbos 2000; Oey et al. 2007; Barnes et al. 2021). As images, we use the spatially resolved face-on projections with two different resolutions: 50 pc to mimic MUSE-like resolution and 1.5 kpc to model MANGA-like resolution of nearby galaxies. The 50 pc H α surface brightness maps are presented in Fig. 1, while the effect of lowering the resolution is shown in Appendix A2. The clumps are identified with `astrodendro` (Robitaille et al. 2019), with a surface brightness threshold of 10^{32} erg s^{-1} pc^{-2}, a minimum height for a leaf to be considered an independent entity of 5, and a minimum number of pixels for a leaf to be considered an independent entity of 10 (pixel size of 10 pc). Varying these parameters by an order of magnitude did not affect our results significantly (i.e. $f_{\rm DIG}$ changed by less than 10 per cent), i.e. the clump finding with this method is robust.

In Fig. 9, we plot the fraction of the H α Balmer emission originating from DIG, $f_{\rm DIG}$, as a function of the H α surface brightness, which is defined as

$$\Sigma_{\rm H\alpha} = \frac{L_{\rm H\alpha}^{\rm tot}}{2\pi R_{\rm half,H\alpha}^2}, \quad (4)$$

where $L_{\rm H\alpha}^{\rm tot}$ is the total H α luminosity and $R_{\rm half,\,H\alpha}$ is the half-light radius of the galaxy's H α emission. We measure $R_{\rm half,\,H\alpha}$ by determining the radius from the face-on projected maps that encloses half of the total H α flux.

Fig. 9 compares the aforementioned different DIG selection methods. Specifically, the left-hand panel shows the result for our fiducial density cut, while the middle and right-hand panels show the results for the clump finding applied to 50 pc and 1.5 kpc resolution images. In all panels, the red, purple, and teal symbols represent the MW, LMC-BC03, and LMC-BPASS simulations, respectively. The filled symbols show the observed $f_{\rm DIG}$ values, while the open symbols show the intrinsic $f_{\rm DIG}$ values.

The first thing to notice is – regardless of the exact definition of the DIG – that the MW values are more clustered together, while the values for the LMC show more scatter, which is largely driven by the more variable star-formation activity. Furthermore, there is a stark difference between the observed and intrinsic $f_{\rm DIG}$: the observed $f_{\rm DIG}$ is about a factor of 2–3 larger than the intrinsic $f_{\rm DIG}$. This makes sense physically since the DIG H α photons are emitted in less dense regions, which allows those photons to escape more easily, while the H II photons are more likely to be absorbed by dust locally. Investigating the effects of different DIG selection methods, we find that the clump finding approach typically leads to smaller observed $f_{\rm DIG,\,obs}$ values, but similar intrinsic $f_{\rm DIG,\,int}$ values, in comparison with our fiducial density-based method. Decreasing the resolution of the images to which the clump finding is applied to leads to an increase of the DIG fraction since high-surface brightness clumps are more smeared out. The exact quantitative values can be found in Table 2.

In addition, we perform an approximate comparison to observations from the SINGG H α survey (Oey et al. 2007) and the PHANGS-MUSE survey (Belfiore et al. 2022; Emsellem et al. 2022) in Fig. 9. We emphasize that this is only a 'rough' comparison because it is difficult to mimic the same method as adopted in the observations, such as modelling the exact noise properties of the observational data and the data processing (i.e. binning of pixels in order to achieve a homogeneous signal-to-noise ratio). Oey et al. (2007) showed that $f_{\rm DIG}$ decreases with increasing $\Sigma_{\rm H\alpha}$. Specifically, they argue that H II regions occupy a larger fraction of the ionized ISM volume as star formation becomes more concentrated, predicting a dependence of $f_{\rm DIG} \propto \Sigma_{\rm H\alpha}^{1/3}$. This agrees well with data from the SINGG H α survey (grey plus symbols in Fig. 9). Sanders et al. (2017), using the data from Oey et al. (2007), fitted $f_{\rm DIG}$ as a function of $\Sigma_{\rm H\alpha}$, obtaining:

$$f_{\rm DIG} = -1.5 \times 10^{-14} \times \Sigma_{\rm H\alpha}^{1/3} + 0.748, \quad (5)$$

where $\Sigma_{\rm H\alpha}$ is in units of erg s^{-1} kpc^{-2}. This best fit is shown as the solid grey curves in Fig. 9. Recently, the higher resolution data from the PHANGS-MUSE survey (Belfiore et al. 2022) point towards a lower DIG fraction than what Oey et al. (2007) reported at fixed $\Sigma_{\rm H\alpha}$. Those observations are shown as dark grey crosses in Fig. 9. Specifically, in the MW range of $\Sigma_{\rm H\alpha}$ Oey et al. (2007)

Table 2. DIG fraction of the Balmer H α emission for different DIG selection method: our fiducial density selection selection versus clump finding with different resolutions. We also differentiate between the observed (obs) and intrinsic (int) emission.

Simulation	Density selection $f_{\rm DIG,\,obs}$	Density selection $f_{\rm DIG,\,int}$	Clump finding (50 pc) $f_{\rm DIG,\,obs}$	Clump finding (50 pc) $f_{\rm DIG,\,int}$	Clump finding (1.5 kpc) $f_{\rm DIG,\,obs}$	Clump finding (1.5 kpc) $f_{\rm DIG,\,int}$
MW	$0.59^{+0.10}_{-0.08}$	$0.24^{+0.09}_{-0.07}$	$0.44^{+0.08}_{-0.04}$	$0.23^{+0.09}_{-0.07}$	$0.42^{+0.12}_{-0.10}$	$0.37^{+0.11}_{-0.13}$
LMC-BC03	$0.49^{+0.22}_{-0.17}$	$0.26^{+0.21}_{-0.13}$	$0.32^{+0.12}_{-0.13}$	$0.19^{+0.11}_{-0.09}$	$0.50^{+0.18}_{-0.21}$	$0.45^{+0.23}_{-0.19}$
LMC-BPASS	$0.66^{+0.19}_{-0.23}$	$0.39^{+0.23}_{-0.17}$	$0.43^{+0.15}_{-0.17}$	$0.42^{+0.12}_{-0.10}$	$0.37^{+0.32}_{-0.19}$	$0.33^{+0.33}_{-0.18}$

report a median of $f_{\rm DIG} = 0.66^{+0.13}_{-0.12}$, while Belfiore et al. (2022) find $f_{\rm DIG} = 0.42^{+0.11}_{-0.05}$ (see also Chevance et al. 2020, who estimate the DIG fraction of a subsample of PHANGS galaxies using H α narrow-band data, finding overall consistent results with Belfiore et al. 2022). This observational difference indicates that there is not yet a consensus and different observational methods and data sets can easily lead to differences on the 10–20 per cent level. Nevertheless, we find that our MW simulation agrees very well with the more recent PHANGS-MUSE observations when adopting the clump finding method with 50 pc resolution data ($f_{\rm DIG,obs} 0.44^{+0.08}_{-0.04}$ in the simulation versus $0.42^{+0.11}_{-0.05}$ in the observations). The LMC-BC03 and LMC-BPASS simulations are consistent with the observations as well, but it is more difficult to make a more conclusive statement due to the scarcity of the observational data and the overall large scatter (in both observations and simulations). Obviously, a more rigorous comparison between simulations and observations is needed in the future. Furthermore, investigating other DIG selection methods (for example based on the emission line [S II]) is also of great interest (Section 6.2).

Looking further into the different DIG selection methods at hand in this work, it is clear that the clump finding identifies some DIG region photons as stemming from H II regions, which leads to a lower DIG fraction with respect to the physical density cut. We show this explicitly in Fig. 10 for the MW simulation, which plots the normalized distribution of $f_{\rm DIG}$ for DIG and H II regions as identified by the clump finding method on images with 50 pc (thick red and blue lines) and 1.5 kpc (thin orange and bright blue lines) resolution. Here, $f_{\rm DIG}$ refers to our fiducial density-based method and has been estimated for each spatial region separately. We only consider spatial regions above a surface brightness of 10^{30} erg s^{-1} kpc^{-2}, motivated by observations (e.g. Belfiore et al. 2022). The errorbars indicate the 16–84th percentile of the distribution when considering all snapshots. As clearly shown in the case for the high-resolution analysis, some clumpy features that are identified as H II regions actually have a high $f_{\rm DIG}$, while the diffuse regions (non-clumps) indeed correspond to regions of high $f_{\rm DIG}$. This explains the aforementioned difference (see also Fig. 9). When lowering the resolution, there is much more mixing, leading to H II regions with high $f_{\rm DIG}$.

Finally, we focus on the H α EW distribution of the DIG and H II emission. Some observational studies (e.g. Lacerda et al. 2018; Vale Asari et al. 2019) define regions with low EW of H α emission (e.g. EW(H α) < 3 Å) as DIG. The motivation from this stems form the fact that EW(H α) can distinguish between ionization due to hot low-mass evolved stars ('HOLMES'; low- to intermediate-mass stars with 0.8–8 $M_\odot$ in all stages of stellar evolution subsequent to the AGB) from that of star formation (and AGN). The exact boundary between HOLMES and star formation depends on metallicity, IMF, and stellar evolution tracks, but it has been put forward that HOLMES typically produce EW(H α) of 0.5–2.5 Å (e.g. Cid Fernandes et al. 2014; Byler et al. 2019). Inspired both by theoretical and empirical considerations, Lacerda et al. (2018) suggested a three-tier scheme: regimes where EW(H α) < 3 Å are dominated

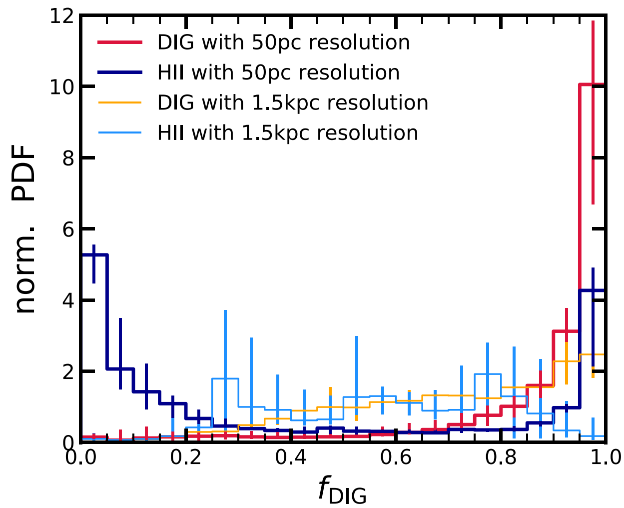

Figure 10. Comparison of the different DIG selection methods on spatially resolved scales. We plot the normalized distribution of $f_{\rm DIG}$, as defined by our fiducial density threshold method, for DIG and H II regions as identified by the clump finding method on images with 50 pc (thick red and blue lines) and 1.5 kpc (thin orange and bright blue lines) resolution. The errorbars indicate the 16–84th percentile of the distribution when considering all snapshots. The diffuse regions (non-clumps) indeed correspond to regions of high $f_{\rm DIG}$. However, some clumpy features that are identified as H II regions actually have a high $f_{\rm DIG}$, which leads to the overall lower $f_{\rm DIG}$ in the clump finding method in comparison with the density selection method as shown in Fig. 9. Lowering the resolution of the clump finding method leads to more mixing.

by HOLMES (i.e. DIG), regions where EW(H α) > 14 Å trace star-formation complexes (i.e. H II regions), and the intermediate regions with EW(H α) = 3–14 Å reflect a mixed regime.

An important consideration in the discussion of the EW(H α) on spatially resolved scales is – in addition to spatial resolution – the size of the aperture. In particular, is the EW calculated over individual pixels or binned pixels (according to some signal-to-noise criterion or some classification schema, such as DIG versus H II regions)? Since the EW is a ratio quantity, calculating the EW for individual or binned pixel can have an important effect, as we highlight now.

Fig. 11 plots the normalized EW(H α) distributions for the DIG and H II regions in red and blue, respectively. In the left-hand panel, we use our fiducial physical DIG definition that is based on a density cut of the emitting gas to identify DIG regions in the face-on projection ($f_{\rm DIG} > 0.5$). In the middle and right-hand panel, we identified H II region with the clump finding method described above. These distributions depend not only on the DIG definition, but also on the aperture over which the EW are calculated: the red and blue histograms (together with the vertical lines indicating the median and 16–84th percentile of the distributions) estimate the EW over

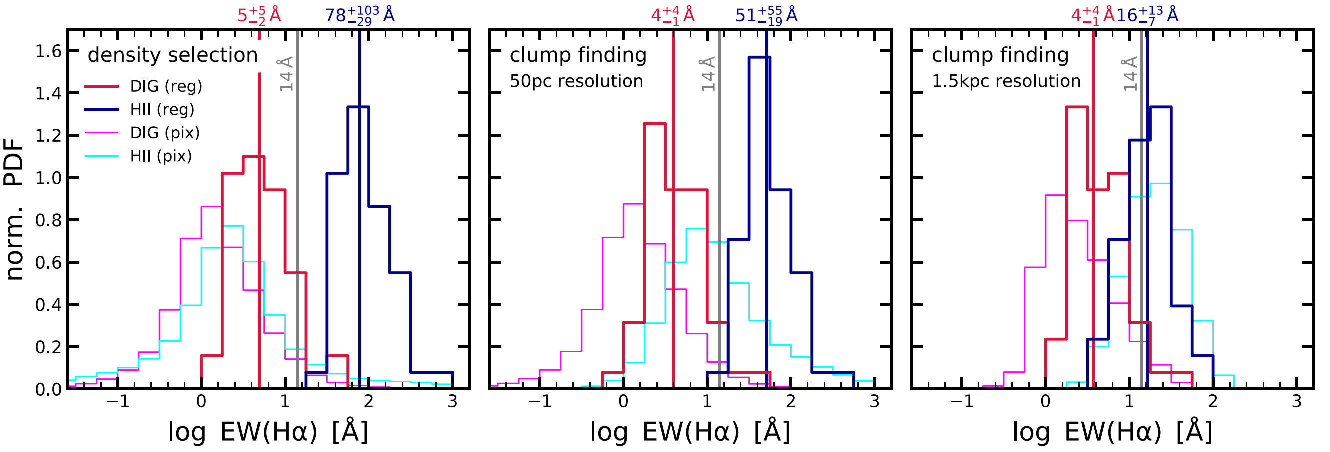

Figure 11. H α EW distributions for the DIG (red) and H II (blue) regions as identified by the different selection methods. From left to right we show the results for our fiducial physical DIG definition that is based on a density cut of the emitting gas, and clump finding on images with 50 pc and 1.5 kpc resolution. These distributions depend not only on the DIG definition, but also on the aperture over which the EW are calculated: the red and blue histograms (together with the vertical lines indicating the median and 16–84th percentile of the distributions) estimate the EW over the entire DIG and H II regions (reg), while the magenta and cyan histograms show the EW of all the individual 10 pc × 10 pc pixels classified as either DIG or H II (pix). The vertical grey lines indicate 14 Å, suggested by Lacerda et al. (2018) as a cut to select pure H II regions.

the entire DIG and H II regions ('reg', i.e. binned pixels), while the magenta and cyan histograms show the EW of all the individual 10 pc × 10 pc pixels classified as either DIG or H II (pix). We find that this pixel binning affects the distributions significantly, in particular in case of high-resolution data. Binning individual pixels together leads to a bias towards the brightest pixels, hence higher EWs. This effect makes it difficult to perform a robust comparison to observations, since observers typically bin pixels in a non-homogeneous manner in order to achieve an optimal arrangement of signal-to-noise ratios. Quantitatively, we find, when calculating the EW over entire DIG and H II regions, EW(Hα) = 5^{+5}_{-2} Å for the DIG and EW(Hα) = 78^{+103}_{-29} Å for the H II regions when performing our fiducial density selection (left-hand panel of Fig. 11). Adopting the clump finding method on 50 pc data (middle panel) leads to similar EWs (DIG EW(Hα) = 4^{+4}_{-1} Å for DIG and EW(Hα) = 51^{+55}_{-19} Å for H II regions). In both cases, a value of 14 Å (vertical grey line) seems to work well for selecting pure H II regions, which is consistent with Lacerda et al. (2018). Furthermore, the 50 pc clump finding results are in excellent agreement with the quoted values from the PHANGS-MUSE survey (Belfiore et al. 2022): EW(Hα) = $5.3^{+12.1}_{-3.0}$ Å for the DIG and EW(Hα) = $48.7^{+98.4}_{-34.0}$ Å for the H II regions. Lowering the resolution (right-hand panel) leads to more mixing and a smaller difference in the EWs of the DIG and H II regions. Specifically, the EW threshold to identify H II region needs to be lowered.

Focusing on the effect of binning, we find that EW distributions are significantly lower when evaluating individual pixels. This effect is particularly drastic when considering high-resolution data: EW(H α) = $1.5^{+0.7}_{-0.4}$ Å for the DIG and EW(H α) = $2.1^{+0.5}_{-0.2}$ Å for the H II regions when performing our fiducial density selection, while EW(H α) = $1.5^{+0.5}_{-0.4}$ Å for the DIG and EW(H α) = $12.5^{+4.0}_{-1.9}$ Å for the H II regions when adopting the 50 pc clump finding. The reason for this is that the faint H α regions (EW(H α) < 1 Å; regions where stars are present but nearly no H α emission) are binned into larger regions, where their contribution is insignificant. The overall effect is that the long tail to low EWs is binned up and high EW regions dominate. Additionally, adopting the clump finding method leads to a larger difference on the individual pixels than for the density selection, with H II regions having an EW(H α) that is roughly an order-of-magnitude larger than the DIG regions. This is not surprising, because the clump finding method by definition classifies regions of high H α surface brightness as H II regions, which typically also have a higher EW(H α).

In summary, although different selection techniques lead to quantitative different DIG fractions, we find that the observed DIG fraction is of the order of ∼ 50 per cent. Importantly, the intrinsic DIG fraction (i.e. before accounting for dust absorption and scattering) is a factor of 2–3 times lower. The H α EW is not a good tracer of whether an H α photon has been emitted in dense gas (H II region) or diffuse gas (DIG region). A key question that we have not yet addressed in the section is: *What powers the DIG?* We find that leaking radiation from H II regions can play a major role. As shown in our companion paper (fig. 25 in Smith et al. 2021), in the MW simulation about 30 per cent of all the LyC photons travel 0.01–1.0 kpc before they ionize hydrogen (or undergo dust absorption), with an additional 15 per cent travelling beyond 1 kpc.[4] This radiation is in principle enough to power an intrinsic DIG fraction of 20–30 per cent as required. Nevertheless, we find that additional processes such as collisional excitation and ionization (related to, e.g. shocks) also contribute to the H α emission on the 5–10 per cent level and therefore can contribute substantially to the powering of the DIG (Section 5.2). As shown in Appendix B, older stars (>10^8 yr) contribute to ≈ 2 per cent the ionizing budget of the MW simulation (this increases to ≈ 8 per cent for the LMC simulation assuming the BC03 SPS model) and therefore do not dominate the DIG emission in these simulations. This has implications for the high-ionization lines (e.g. Zhang et al. 2017), which is of great interest for upcoming studies (Section 6.2).

4.6 Extraplanar Balmer emission

We now focus on understanding the origin of the extraplanar Balmer emission, which is directly related to the previous discussion about the DIG. As we have highlighted in the Introduction, there are two

[4] About 6 per cent of the LyC radiation escapes the galaxy.

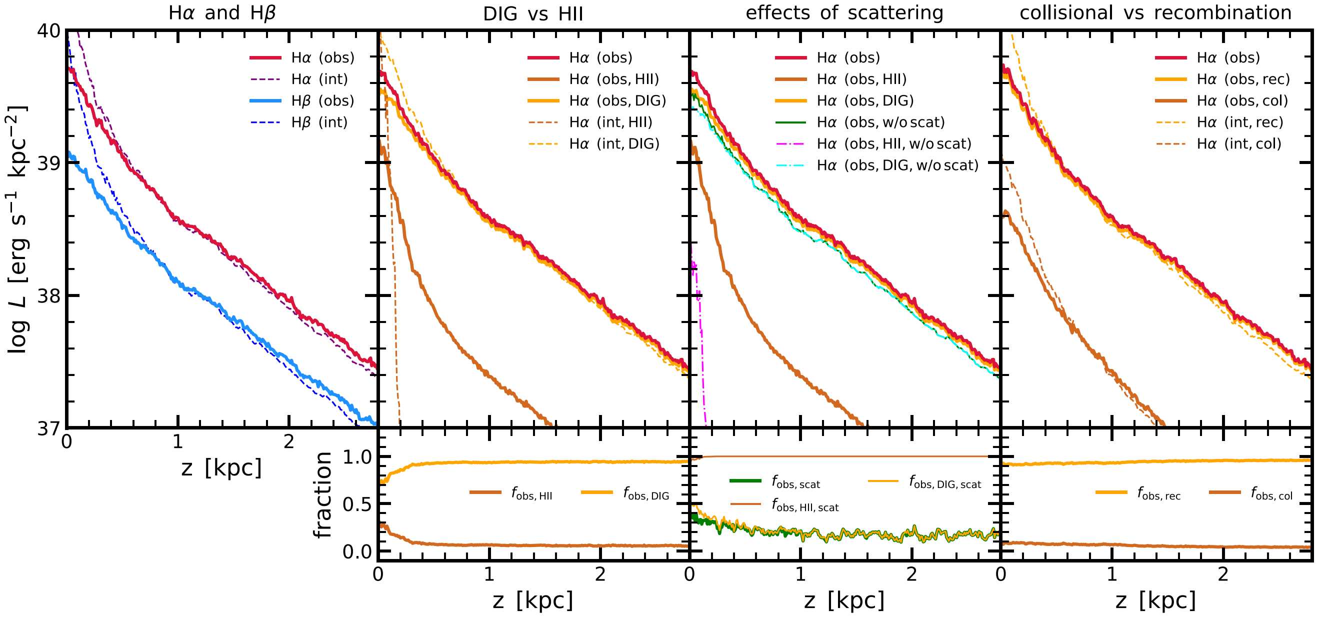

Figure 12. Extraplanar Balmer emission of the MW simulation. From left to right, the vertical profiles of H α and H β, of H α split by DIG and H II photons, of H α split by scattered and non-scattered photons, and H α split by radiative recombination and collisional excitation. The smaller panels on the bottom show the fractional contribution of the different components. All the vertical profiles are obtained within the effective radius of 4.3 kpc. The key message from this figure is that the Balmer emission at large scale heights ($z > 200$ pc) is mainly emitted *in situ* via radiative recombination, emitted in low-density gas (i.e. the DIG), and scattering is significant but not dominant ($f_{\rm scat} \approx 20$ per cent).

possible explanations for this extraplanar emission. On one hand, this emission could be produced by ionizing photons transported through transparent pathways carved out by superbubbles or chimneys. On the other hand, it could be caused by dust scattering of the photons originating from H II regions in the galactic disc. Motivated by the good agreement between the scale heights of our simulated MW galaxy and the observations (Section 3.2), we now investigate the physical origin of this extraplanar Balmer emission.

In Fig. 12, we show the vertical profiles within the effective radius of 4.3 kpc for the MW simulation split by different diagnostics. The left-hand panel shows the vertical profiles for H α and H β emission. The solid and dashed lines show the observed and intrinsic emission, respectively. As expected, the intrinsic profile is nearly 1 dex higher than the observed profile within the disc ($z < 200$ pc), which can be explained by the absorption of dust. There is very little difference between the intrinsic and observed emission at high altitudes: the observed emission is slightly above (<0.2 dex) the intrinsic emission because of scattering (see below).

The second panel from the left in Fig. 12 splits the H α emission by photons emitted in H II regions and the DIG, as defined by the simple gas density cut ($n_{\rm thresh} = 100$ cm^{-3}). We find that the DIG dominates at all scale heights. The fraction of H α photons emitted by the DIG is $f_{\rm DIG}$ 70 per cent within the disc (see lower panel) and increases towards larger heights to $f_{\rm DIG} > 90$ per cent. There is very little difference between the intrinsic and observed emission for the DIG component. Contrarily, the intrinsic H II photons are basically all emitted within the disc ($z < 200$ pc), while they are observed out to much higher scale heights ($z > 1$ kpc). This can be explained by dust scattering, as we discuss next.

In the third panel from the left in Fig. 12 we investigate the importance of scattering of H α photons. This shows that indeed all (∼ 100 per cent) of the H II photons at large scale heights have been scattered. Looking at DIG photons, we find that scattering is significant with a fraction of 10–30 per cent. Since the DIG photons dominate, we find that the majority of extraplanar H α emission is not scattered ($f_{\rm scat} \approx$ 10–30 per cent).

Finally, in the rightmost panel of Fig. 12 we split the H α emission by the physical emission process, i.e. radiative recombination and collisional excitation. We find that at all scale heights, radiative recombination clearly dominates.

In summary, the extraplanar emission extends to several kpc in our MW simulation. The exponential scale height amounts on average to 0.7 kpc, consistent with observations (see Fig. 4). As shown in Fig. 12, this extraplanar Balmer emission is produced *in situ* by ionizing photons emitted from the disc via radiative recombination. Those ionizing photons must be transported through transparent pathways carved out by superbubbles or chimneys (see Fig. 1). This is consistent with our measurement that about 30 per cent of all the LyC photons travel 0.01–1.0 kpc before they ionize hydrogen (see fig. 25 of our companion paper, Smith et al. 2021). Since the gas density is low at large scale heights, we classify all of this Balmer emission as being emitted from the DIG. We find that scattering increases the H α luminosity above the plane of the disc by roughly $f_{\rm scat} \approx$ 10–30 per cent.

5 BALMER LINES AS A STAR-FORMATION TRACER

H α is a prime indicator for the SFR of galaxies, both on global and spatially resolved scales (see Introduction). We now turn to understanding the connection between the SFR and H α in more detail. In particular, we look into the time evolution of H α and SFR (Section 5.1), the connection between the intrinsic H α emission and the SFR (‘conversion factor’; Section 5.2), dust correction (Section 5.3), and star-formation time-scale probed by H α (Section 5.4).

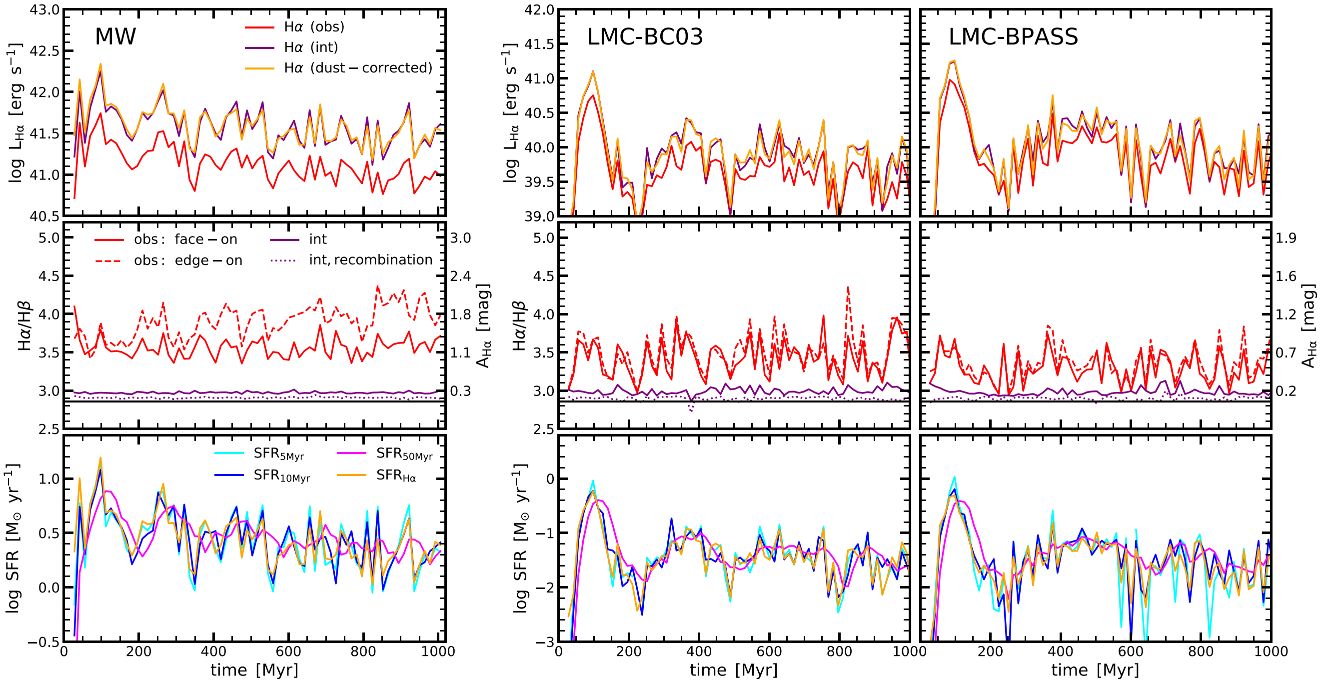

Figure 13. Time evolution of the H α luminosity (top panels), Balmer decrement (ratio of the observed H α/H β in the middle panels), and the SFR (bottom panels) for the MW (left-hand panels), LMC-BC03 (middle panels), and LMC-BPASS (right-hand panels) simulations. All quantities are measured within an aperture of 15 kpc. The red, purple, and orange lines in the top panel show the observed, intrinsic, and dust-corrected (using the Balmer decrement) H α luminosities. The Balmer decrement oscillates around a typical value of ∼3.5, which corresponds to an attenuation for H α of $A_{H\alpha} \approx 1.0$ mag. The SFR is estimated considering stars with ages $t_{age} < 5$ Myr (cyan), <10 Myr (blue), and <50 Myr (pink). The orange line in the bottom panel shows the SFR estimated from the dust-corrected H α luminosity using the Balmer decrement, which closely follows the SFR averaged over short time-scales (<5–10 Myr).

5.1 Time evolution of the H α luminosity and SFR

In Fig. 13, we show the temporal evolution of the H α luminosity (top panels), Balmer decrement (ratio of the observed H α/H β in the middle panels), and the SFR (bottom panels) for the MW (left-hand panels), LMC-BC03 (middle panels), and LMC-BPASS (right-hand panels) simulations. All measurements are on global scales; i.e. obtained with an aperture of 15 kpc. For the H α luminosity, we plot the observed luminosity (red line), intrinsic luminosity (without dust absorption and scatter; purple line), and dust-corrected luminosity (orange line), which we perform via the Balmer decrement as described in Section 5.3. As we see, for all simulations, the dust correction works extremely well and is able to recover the intrinsic H α luminosity nearly perfectly.

In the middle panels of Fig. 13, we show the Balmer decrement for face-on and edge-on views as red solid and dashed lines, respectively. In the MW case, we can clearly see that the edge-on alignment exhibits a larger Balmer decrement, which is consistent with the idea that edge-on integrations lead to higher attenuation (by about 0.5 mag for H α). There is very little difference between the different sightlines in the LMC simulations due to the lower dust content. In these middle panels, we also plot the intrinsic Balmer decrement as solid purple lines. We find on average an intrinsic Balmer decrement of $(\mathrm{H}\alpha/\mathrm{H}\beta)_{\mathrm{int}} = 2.97^{+0.01}_{-0.01}$, $2.99^{+0.05}_{-0.04}$, and $2.97^{+0.04}_{-0.03}$ for the MW, LMC-BC03, and LMC-BPASS simulations; all values are close to the fiducial value of 2.87 (shown as vertical black line) that assumes an electron temperature of $T_e = 10^4$ K, an electron density of $n_e = 10^2$ cm^{-3}, and Case B recombination conditions (Osterbrock & Ferland 2006). Most of the differences can be explained by collisional excitation emission, which intrinsically has a higher Balmer decrement (the dotted purple line shows the Balmer decrement for the intrinsic radiative recombination radiation), while the rest is due to the more realistic range of different gas temperatures and densities (see Fig. 5).

In the bottom panels of Fig. 13 we plot the SFR estimated from H α (orange line) assuming an effective conversion factor (see the next section) and direct measurements of the SFR by considering all stars born in the past 5 Myr (cyan line), 10 Myr (blue line), or 50 Myr (pink line). The H α-based SFR employs the dust-corrected H α luminosity and an *effective* H α–SFR conversion factor, which we discuss in detail in the next section. We see that the H α-based SFR accurately traces the <5–10 Myr SFR, something we explore more in Section 5.4.

5.2 The Hα–SFR conversion factor

In order to derive an SFR from the observed H α luminosity, two steps are necessary. First, the observed H α luminosity needs to be corrected for dust attenuation to derive the intrinsic H α luminosity. Secondly, the intrinsic H α luminosity needs to be converted to the SFR via an H α-to-SFR conversion factor. We now focus on the H α-to-SFR conversion (i.e. focusing on the relation between the intrinsic H α emission and its relation with star formation) and discuss the dust correction in the next section. For this section, by 'SFR' we mean the SFR considering all stars born in the past 5 Myr (i.e. $\langle \mathrm{SFR} \rangle_{5\mathrm{Myr}}$; Section 5.4).

The intrinsic (or dust-corrected) H α luminosity $L(\mathrm{H}\alpha)_{\mathrm{int}}$ can be converted to an SFR via

$$\mathrm{SFR} = C \times L(\mathrm{H}\alpha)_{\mathrm{int}}, \quad (6)$$

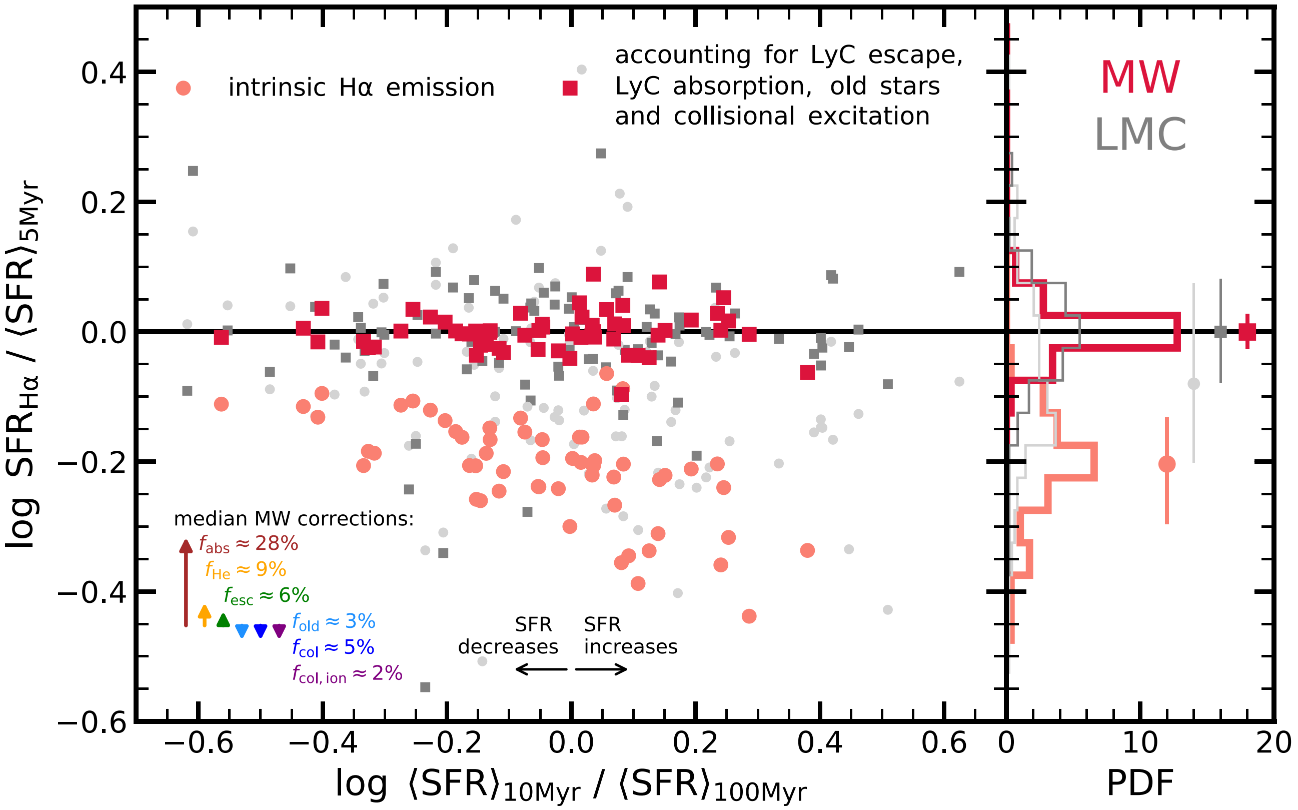

Figure 14. H α–SFR connection. We compute the SFR from the intrinsic H α emission (i.e. no dust absorption) by multiplying it with the Kennicutt (1998) conversion factor (equation 6) and denote it by $\mathrm{SFR}_{\mathrm{H}\alpha}$. We plot the ratio of $\mathrm{SFR}_{\mathrm{H}\alpha}$ and the true SFR (averaged over 5 Myr; $\langle\mathrm{SFR}\rangle_{5\mathrm{Myr}}$) as a function of $\langle\mathrm{SFR}\rangle_{10\mathrm{Myr}}/\langle\mathrm{SFR}\rangle_{100\mathrm{Myr}}$, which indicates whether the SFR is increasing or decreasing over the past 100 Myr. The salmon and red symbols are from the MW simulations, while the grey symbols are from both the LMC-BC03 and LMC-BPASS simulations. We find that the simple H α-based SFR underpredicts the true SFR by $0.20^{+0.09}_{-0.07}$ ($0.05^{+0.12}_{-0.12}$ and $0.12^{+0.11}_{-0.24}$) dex in the MW (LMC-BC03 and LMC-BPASS) case. For the MW simulation, this can be explained by the dust and helium absorption of ionizing LyC photons ($f_{\mathrm{abs}} \approx 28$ per cent and $f_{\mathrm{He}} \approx 9$ per cent), while effects related to the escape of LyC photons and H α emission collisionally excited gas roughly cancel each other out ($f_{\mathrm{esc}} \approx 6$ per cent versus $f_{\mathrm{col}} \approx 5$ per cent), see arrows in the lower left for the average strengths of these processes. Contributions from older stars ($f_{\mathrm{old}} \approx 3$ per cent) and collisionally ionized gas ($f_{\mathrm{col,\,ion}} \approx 2$ per cent) are both small. Since the f_{abs} depends on the recent SFH, these corrections are actually dependent on the SFH itself.

where C is the H α-to-SFR conversion factor. This factor typically assumes that: (i) the star formation has been roughly constant over the time-scale probed (in case of H α a few tens of Myr), (ii) the stellar IMF is known, and (iii) the stellar IMF is fully sampled. Furthermore, in the case of nebular lines such as H α, values for the electron temperature and density also need to be assumed. Not surprisingly, there is a significant variation among published calibrations ($\sim$ 30 per cent), with most of the dispersion reflecting differences in the stellar evolution and atmosphere models. We adopt for the MW simulation $C = 4.5 \times 10^{-42}\,(\mathrm{M}_{\odot}\ \mathrm{yr}^{-1})/(\mathrm{erg\ s}^{-1})$, which is consistent – after converting from a Salpeter (1955) to a Chabrier (2003) IMF using the conversion presented in Driver et al. (2013) – with the widely used conversion factor of Kennicutt (1998). The conversion factor of the LMC-BC03 and LMC-BPASS simulations (both 0.5 $\mathrm{Z}_{\odot}$) are taken to be 4.2 and $2.1 \times 10^{-42}\,(\mathrm{M}_{\odot}\ \mathrm{yr}^{-1})/(\mathrm{erg\ s}^{-1})$, respectively.

We now convert the intrinsic H α luminosities to SFRs via equation (6) with the aforementioned standard Kennicutt (1998) conversion factor. We compare these SFRs ($\mathrm{SFR}_{\mathrm{H}\alpha}$) with the SFR obtained by considering all stars born in the previous 5 Myr; i.e. the true SFR averaged over the previous 5 Myr; $\langle\mathrm{SFR}\rangle_{5\mathrm{Myr}}$. Specifically, in Fig. 14 we show the ratio of the H α-based SFR and the true SFR of the simulation as a function of the ratio of the true SFR averaged over the previous 10 Myr and the previous 100 Myr; i.e. the x-axis shows whether the star-formation history (SFH) is increasing or decreasing over the past 100 Myr.

The salmon-coloured (bright grey) points in Fig. 14 are obtained by adopting the H α-based SFR of the MW (LMC-BC03 and LMC-BPASS) simulation with the simple conversion described above. We clearly see that these points lie below the black vertical line, indicating that the SFRs obtained from the intrinsic H α luminosity are systematically underestimating the true SFR averaged over the previous 5 Myr. In fact, there is a trend with the SFH evolution in which snapshots where the SFH over the past 100 Myr was increasing have H α-based SFRs that are 0.2–0.4 dex lower than the true SFR. This difference is only about 0.1 dex when the SFH is decreasing. The median difference for the MW, LMC-BC03, and LMC-BPASS simulations is $-0.20^{+0.07}_{-0.09}$, $-0.05^{+0.12}_{-0.12}$, and $-0.12^{+0.24}_{-0.11}$, respectively. The difference is typically less for the LMC than for the MW simulation. What is the reason for this difference?

As shown in Fig. 2, there are several different physical processes that can reduce or boost the H α luminosity relative to the SFR; i.e. the formation rate of young stars. First, ionizing LyC photons from young massive stars can be absorbed by dust and helium before ionizing hydrogen that recombines to emit H α photons. This reduction of

H α production relative to the SFR is significant in our simulations: we find (median over all snapshots) that $f_{\rm abs} \approx 28$ per cent of LyC photons are absorbed by dust, while $f_{\rm He} \approx 9$ per cent of LyC photons ionizing helium.[5] Secondly, some ionizing LyC photons escape the galaxy and do not interact with either gas or dust. The fraction of escaping LyC photons is low with an average of $f_{\rm esc} \approx 6$ per cent. Thirdly, as discussed in Section 4.2, collisionally excited gas actually boosts the H α emission relative to the SFR, though this fraction is low with an average of $f_{\rm col} \approx 5$ per cent. Directly related to this is the collisionally ionized gas which contributes negligibly with $f_{\rm col,ion} \approx 2$ per cent. Fourthly, older stars with ages of >10 Myr only weakly boost the H α luminosity on the level of $f_{\rm old} \approx 3$ per cent. Finally, one more channel that is self-consistently modelled is photoionization by the UV background, which produce very little recombination emission (< 1 per cent), which we therefore do not report here.

These corrections are different for the LMC simulations: ($f_{\rm abs}$, $f_{\rm He}$, $f_{\rm esc}$, $f_{\rm col}$, $f_{\rm col,\,ion}$, $f_{\rm old}$) are on average (12 pe cent, 11 per cent, 5 per cent, 7 per cent, 4 per cent, 8 per cent) and (15 per cent, 6 per cent, 12 per cent, 6 per cent, 2 per cent, 9 per cent) for the LMC-BC03 and LMC-BPASS simulation, respectively. This means that the budget of H-ionizing LyC photons is reduced to $f_{\rm H} \approx 57$ per cent (i.e. 43 per cent of the produced LyC photons are absorbed by dust or helium, or escape the galaxy) in the MW simulation, to $f_{\rm H} \approx 72$ per cent in the LMC-BC03 simulation, and to $f_{\rm H} \approx 67$ per cent in the LMC-BPASS simulation. As expected, the LyC photon absorption by dust is less important for the LMC, while the contribution of older stars is more prominent since the specific SFR of the LMC is lower than that of the MW. Comparing BC03 with BPASS, we find that the LyC escape fraction of the LMC-BPASS model is about twice as high as for the LMC-BC03 model, which can be attributed to the LyC emission of slightly older stellar populations in the former model, which are typically located in less obscured regions of the galaxy.

After correcting each individual snapshot for these effects – the typical arrows of corrections for the MW simulation are shown in the bottom left of Fig. 14 – we find that the H α-based SFR agrees well with the true SFR. The corrected values for the MW (LMC-BC03 and LMC-BPASS) simulation are shown as red-coloured (dark grey) squares in Fig. 14. We find the log difference to be $\log({\rm SFR}_{{\rm H}\alpha,{\rm int}}/\langle{\rm SFR}\rangle) = 0.00^{+0.03}_{-0.03}$, $0.00^{+0.07}_{-0.04}$, and $0.00^{+0.18}_{-0.09}$ for the MW, LMC-BC03, and LMC-BPASS simulations, respectively. Importantly, we find that these aforementioned corrections depend on the SFH, i.e. the ratio of the SFR averaged over 10 and 100 Myr (x-axis of Fig. 14). This makes it difficult to correct for those effects in practice. Nevertheless, we can define an *effective* conversion factor, which takes into account these corrections on average. Specifically, we find $C_{\rm eff} = 7.1$, 4.7, and 2.7×10^{-42} (M$_\odot$ yr^{-1})/(erg s^{-1}) for the MW, LMC-BC03, and LMC-BPASS simulation, respectively. These effective conversion factors lead to $\log({\rm SFR}_{{\rm H}\alpha,{\rm int}}/\langle{\rm SFR}\rangle) = 0.00^{+0.07}_{-0.09}$, $0.00^{+0.12}_{-0.12}$, and $0.00^{+0.24}_{-0.11}$, implying that there is little bias in estimated SFRs though the dispersion increases significantly.

In summary, to reproduce the true SFR averaged over 5 Myr in the simulation from the intrinsic H α emission, we need to include a correction factor to account for the dust and helium absorption, the escape of LyC photons, collisional excitation and ionization emission, and the contribution from older stars. This correction can be achieved by increasing the H α-to-SFR conversion factor by ∼ 50 per cent (10–30 per cent) in the MW (LMC) simulation. Absorption of LyC photons is challenging to measure observationally, but it has been highlighted as a caveat in the literature (e.g. Puglisi et al. 2016; Tacchella et al. 2018). Salim et al. (2016), fitting ∼ 700 000 local galaxies with CIGALE, found a fraction of LyC photons absorbed by dust to be 0.3 in order to match the observed EWs of the main optical lines (H α, H β, [O II], [O III]) from SDSS spectra. Consistently, previous studies on nearby spiral galaxies found similar LyC photon absorption fractions of 0.3–0.5 (Inoue, Hirashita & Kamaya 2001; Hirashita, Buat & Inoue 2003; Iglesias-Páramo et al. 2004). This is in good agreement with our inferred absorption and escape of a total of ∼ 43 per cent ($f_{\rm abs} \approx 28$ per cent due to dust absorption, $f_{\rm He} \approx 9$ per cent due to helium absorption, and $f_{\rm esc} \approx 6$ per cent due to escape), which highlights that the absorption of LyC photons is significant (∼0.1–0.2 dex) and needs to be accounted for when estimating the SFRs from Balmer emission lines. On the theoretical side, using a periodic tall box simulation to explore sub-parsec scale feedback and emission in the solar neighbourhood, Kado-Fong et al. (2020) find approximately half of ionizing photons are absorbed by gas and half by dust, i.e. $f_{\rm abs} \approx 0.5$. This is roughly in the same ballpark as our estimate.

5.3 Balmer decrement and attenuation law

The dust attenuation towards star-forming regions is most directly probed using Balmer recombination line flux ratios, because as dust attenuation is wavelength dependent, its effects can be measured by comparing the observed and intrinsic Balmer decrements (e.g. Calzetti 1997). Specifically, dust will preferentially absorb the shorter wavelength Hβ λ4861 Å line rather than the longer wavelength Hα λ6563 Å line, increasing the observed value of the Balmer decrement $({\rm H}\,\alpha/{\rm H}\,\beta)_{\rm obs}$. The Balmer decrement can therefore be used to derive the attenuation towards H α in the following way:

$$A_{{\rm H}\alpha} = \frac{\kappa(\lambda_{{\rm H}\alpha})}{\kappa(\lambda_{{\rm H}\beta}) - \kappa(\lambda_{{\rm H}\alpha})} \times 2.5 \log \left(\frac{({\rm H}\,\alpha/{\rm H}\,\beta)_{\rm obs}}{({\rm H}\,\alpha/{\rm H}\,\beta)_{\rm int}} \right), \quad (7)$$

where $\kappa(\lambda)$ is the attenuation curve. The intrinsic Balmer decrement $({\rm H}\,\alpha/{\rm H}\,\beta)_{\rm int}$ is not constant for and within galaxies since it depends on both the electron temperature and density and collisional excitation. It is usually assumed to be $({\rm H}\,\alpha/{\rm H}\,\beta)_{\rm int} = 2.87$, which is valid for an electron temperature of $T_{\rm e} = 10^4$ K and an electron density of $n_{\rm e} = 10^2$ cm^{-3}, under Case B recombination conditions (Osterbrock & Ferland 2006). However, with higher temperature or higher density, we expect that $({\rm H}\,\alpha/{\rm H}\,\beta)_{\rm int}$ increases since higher temperature or higher density introduces more collisional mixing of electron states, therefore increasing the ability to populate the $n = 4$ state (and thus H β). For typical star-forming regions, Osterbrock & Ferland (2006, see also Dopita & Sutherland 2003) find that increasing $T_{\rm e}$ from 5×10^3 to 2×10^4 K reduces $({\rm H}\,\alpha/{\rm H}\,\beta)_{\rm int}$ from 3.05 to 2.76 at constant $n_{\rm e} = 10^2$ cm^{-3}. At constant $T_{\rm e} = 10^4$ K, $({\rm H}\,\alpha/{\rm H}\,\beta)_{\rm int}$ only reduces from 2.85 to 2.81 for a change in $n_{\rm e}$ from 10^4 to 10^6 cm^{-3}. Therefore, $({\rm H}\,\alpha/{\rm H}\,\beta)_{\rm int}$ is expected to be in the rather narrow range of 2.76 to 3.05.

As described in Section 5.1, the middle panels of Fig. 13 show the observed and intrinsic Balmer decrement as a function of time. We find on average an intrinsic Balmer decrement of $({\rm H}\alpha/{\rm H}\beta)_{\rm int} = 2.97^{+0.01}_{-0.01}$ for the MW and $2.98^{+0.05}_{-0.02}$ for the LMC. This is slightly higher than the aforementioned fiducial value of 2.87. Most of this difference can be explained by collisional excitation emission, which intrinsically has a higher Balmer decrement, while the rest is due to a different gas temperature and gas density than the fiducial one ($T_{\rm e} = 10^4$ K and $n_{\rm e} = 10^2$ cm^{-3}; Fig. 5).

[5] Most of the LyC photons absorbed by helium are actually absorbed by He I, producing He II. We track He II absorption as well (producing He III), though this fraction is about eight times lower than He I absorption.

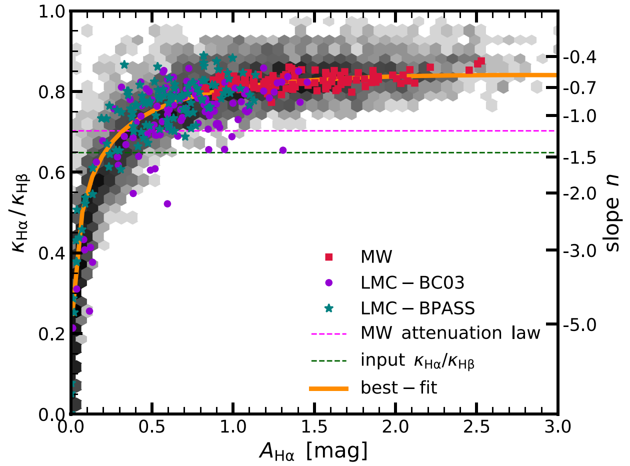

Figure 15. Inferred dust attenuation law for Balmer lines (ratio of the attenuation law function at H α and H β [$\kappa_{H\alpha}/\kappa_{H\beta}$] on the left and the power-law slope n on the right) as a function of the attenuation at H α ($A_{H\alpha}$). We solve for the dust attenuation law by inverting equation (7). The red squares, purple circles, and teal stars show the measurements for the MW, LMC-BC03, and LMC-BPASS simulations, respectively. The hex-binned histogram indicates the measurements on spatially resolved scales from random 1 kpc apertures of the MW simulation. The pink and green dashed lines show the MW attenuation law and the input dust opacities (Section 2.2). The orange line indicates the best fit of equation (8). We find that individual snapshots as well as the spatially resolved measurements follow the trend of steeper attenuation laws for less attenuated regions. Furthermore, for the MW simulation, we find a typical power-law attenuation law with an index of $n \approx -0.63$.

In addition to $(\mathrm{H}\alpha/\mathrm{H}\beta)_{\mathrm{int}}$, the second important factor in deriving $A_{H\alpha}$ from equation (7) is the attenuation curve $\kappa(\lambda)$. The attenuation curve for the nebular emission is not well constrained observationally. Our simulations allow us to infer the attenuation law by inverting equation (7) and measuring in the simulations $A_{H\alpha}$ and $(\mathrm{H}\alpha/\mathrm{H}\beta)_{\mathrm{obs}}$, while assuming $(\mathrm{H}\alpha/\mathrm{H}\beta)_{\mathrm{int}}$. In the following text, we assume the fiducial value of $(\mathrm{H}\alpha/\mathrm{H}\beta)_{\mathrm{int}} = 2.87$.

Fig. 15 shows the inferred shape of the attenuation law (ratio of $\kappa(\lambda_{H\alpha})/\kappa(\lambda_{H\beta})$ on the left and power-law index n on the right) as a function of the measured amount of optical depth (attenuation $A_{H\alpha}$). The integrated measurements for the MW and LMC simulations are shown as red squares and purple circles, respectively. The hex-binned histogram indicates the measurement on spatially resolved scales from random, 1-kpc apertures. The pink dashed line indicates the MW attenuation law, which assumes the Cardelli, Clayton & Mathis (1989) Galactic extinction curve, with an update in the near-UV from O'Donnell (1994). The green dashed line marks the ratio of the input dust opacities for H α and H β (Section 2.2).

It is apparent from Fig. 15 that the integrated measurements follow the spatially resolved measurements for all simulation set-ups: the lower the attenuation, the steeper the attenuation law. We quantify this trend with the following equation:

$$\log(\kappa_{H\alpha}/\kappa_{H\beta}) = n\ \log(\lambda_{H\alpha}/\lambda_{H\beta}) = -0.09\ \log(A_{H\alpha})^2 + 0.08\ \log(A_{H\alpha}) - 0.09, \quad (8)$$

where n is the power-law index from $\kappa(\lambda) \propto \lambda^n$. The best-fitting line is shown as orange curve in Fig. 15.

This trend is consistent with the findings of Chevallard et al. (2013), who analysed a diverse series of theoretical attenuation laws and showed that all the studies predict a relationship between the optical depth and attenuation law slope (see also Narayanan et al. 2018; Trayford et al. 2019; Salim & Narayanan 2020). The physical origin for this optical depth–slope relationship was put forward by Chevallard et al. (2013): red light scatters more isotropically than blue. Red photons emitted in the equatorial plane of the galaxy will be more likely to escape, while blue photons have a comparatively increased likelihood of remaining, and subsequently being absorbed. In the low optical depth limit, this corresponds to a steepening of the attenuation curve for face-on directions.

For the MW simulation, we find a typical slope of the attenuation law of $n = -0.63 \pm 0.07$ ($\kappa(\lambda_{H\alpha})/\kappa(\lambda_{H\beta}) = 0.83 \pm 0.02$) and attenuation of $A_{H\alpha} = 1.1^{+0.3}_{-0.2}$ mag. This is consistent with the power-law exponents for the diffuse ISM and natal birth clouds found by Charlot & Fall (2000). For the LMC simulation, we find a larger variation in both the amount of extinction as well as the slope of the attenuation curve. On average, the LMC has typically a steeper attenuation law and a smaller optical depth than the MW with $A_{H\alpha} = 0.6 \pm 0.3$ mag and $\kappa(\lambda_{H\alpha})/\kappa(\lambda_{H\beta}) = 0.77^{+0.05}_{-0.9}$, which corresponds to a slope of $n = -0.87^{+0.22}_{-0.42}$. These numbers do not significantly change when considering the LMC-BPASS run.

We emphasize that although the measurements shown in Fig. 15 are calculated from the face-on projection, there will be little difference when changing the inclination. Specifically, the extreme case of an edge-on projection for the MW leads – as expected – to more attenuation with $A_{H\alpha} = 1.7 \pm 0.4$ mag. Accordingly, the attenuation law is slightly flatter with $n = -0.65^{+0.07}_{-0.06}$ ($\kappa(\lambda_{H\alpha})/\kappa(\lambda_{H\beta}) = 0.82 \pm 0.02$), but as shown in Fig. 15, the slope of the attenuation law roughly remains constant above $A_{H\alpha} > 1$ mag. This universal optical depth–slope relationship is independent of inclination, which is consistent with the theoretical analysis by Chevallard et al. (2013) and observations by Salim, Boquien & Lee (2018, see also Salim & Narayanan 2020 for a review). Similarly, the optical depth–slope relation also holds for spatially resolved scales, as shown by the grey hex-bin histogram in Fig. 15. This is consistent with observations of local galaxies that show intriguing variations within galaxies, with regions of high attenuation exhibiting a shallower attenuation curve (Decleir et al. 2019).

We can use the optical depth–slope relationship (equation 8) and iteratively solve for $A_{H\alpha}$ and n (i.e. $\kappa(\lambda_{H\alpha})/\kappa(\lambda_{H\beta})$) to obtained the dust-corrected H α luminosity. Fig. 16 plots the ratio of the dust-corrected H α luminosity and the intrinsic H α luminosity as a function of $\langle\mathrm{SFR}\rangle_{10\mathrm{Myr}}/\langle\mathrm{SFR}\rangle_{100\mathrm{Myr}}$, which indicates whether the SFR is increasing or decreasing over the past 100 Myr. The red squares, purple circles, and teal stars show the measurements for the MW, LMC-BC03, and LMC-BPASS simulations, respectively. The hex-binned histogram indicates the measurements on spatially resolved scales from random 1 kpc apertures of the MW simulation. We find that the Balmer dust correction works well, independent of the SFH, though there is a significant amount of scatter with ~0.1–0.2 dex. Specifically, the median and the 16–84th percentile of the log difference between $\mathrm{H}\alpha_{\mathrm{dust\text{-}corr}}$ and $\mathrm{H}\alpha_{\mathrm{int}}$ are $-0.02^{+0.10}_{-0.08}$, $0.04^{+0.20}_{-0.13}$, and $-0.01^{+0.13}_{-0.10}$ for the MW, LMC-BC03, and LMC-BPASS simulations, respectively. For the spatially resolved data of the MW, we find $\log(\mathrm{H}\alpha_{\mathrm{dust-corr}}/\mathrm{H}\alpha_{\mathrm{int}}) = 0.05^{+0.11}_{-0.19}$. These numbers are indicated in the right-hand panel of Fig. 16.

5.4 Time-scale of the Hα SFR tracer

As shown in the bottom panels of Fig. 13, the SFR averaged over short time-scales (5–10 Myr) is in better agreement with the H α-based SFR than the SFR averaged over longer time-scales. Understanding the star-formation time-scale that H α traces is of great importance since by comparing H α-based SFRs to SFRs obtained with other

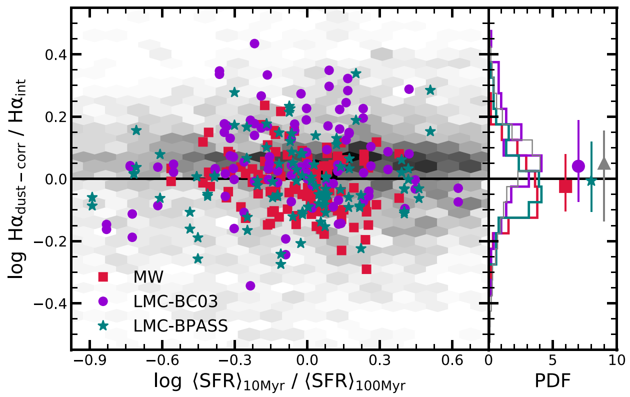

Figure 16. Testing the Balmer decrement dust correction. On the left, we plot the log difference of the H α flux corrected for dust via the Balmer decrement (H $\alpha_{\rm dust\text{-}corr}$; equations 7 and 8) and the intrinsic H α flux (H $\alpha_{\rm int}$) as a function of $\langle{\rm SFR}\rangle_{\rm 10Myr}/\langle{\rm SFR}\rangle_{\rm 100Myr}$, which indicates whether the SFR is increasing or decreasing over the past 100 Myr. The red squares, purple circles, and teal stars show the measurements for the MW, LMC-BC03, and LMC-BPASS simulations, respectively. The hex-binned histogram indicates the measurements on spatially resolved scales from random 1 kpc apertures of the MW simulation. The right-hand panel shows the vertical histogram of log (H $\alpha_{\rm dust\text{-}corr}$/H $\alpha_{\rm int}$), with the medians and the 16–84th percentile indicated with the corresponding symbols and errorbars. The grey triangle shows the median of the random 1 kpc apertures. The Balmer dust correction works well, independent of the SFH, though there is a significant amount of scatter of ∼0.1–0.2 dex.

indicators (for example from the UV continuum), we are able to learn about the variability of star formation (e.g. Sparre et al. 2017; Caplar & Tacchella 2019; Emami et al. 2019). The variability of star formation (sometimes also called 'burstiness') is directly related to how star formation is regulated and it informs us as to what time-scales are important for the evolution of galaxies (Iyer et al. 2020; Tacchella, Forbes & Caplar 2020; Wang & Lilly 2020).

The goal of this section is to determine the time-scale of the H α SFR indicator. We follow the approach outlined in Caplar & Tacchella (2019) and Flores Velázquez et al. (2021). Specifically, we find the best-fitting averaging time-scale $t_{\rm avg,\,min}$ that minimizes the difference between the true SFR $\langle{\rm SFR}\rangle_{t_{\rm avg}}$ of the simulation and the observed SFR ${\rm SFR}_{\rm ind}$. The time-scale $t_{\rm avg,\,min}$ is the width of the boxcar integration over which one would have to average the true SFR of the simulation to match the indicated SFR (in our case H α) at the time of an observation. To find $t_{\rm avg,\,min}$, we minimize the follow root mean square deviation (RMSD) estimate:

$$\mathrm{RMSD}(t_{\rm avg}) = \sqrt{\frac{\sum_i \left(\log \mathrm{SFR}^{i}_{\rm ind} - \log\langle\mathrm{SFR}\rangle^{i}_{t_{\rm avg}}\right)^2}{N}}, \quad (9)$$

where i is the index running over the N snapshots.

In the left-hand panel of Fig. 17 we show the dust-corrected H α SFR (${\rm SFR}_{{\rm H}\alpha,\,{\rm dust\text{-}corr}}$) versus the true SFR ($\langle{\rm SFR}\rangle_{t_{\rm avg}}$), averaged over 5 Myr (cyan), 10 Myr (blue), 50 Myr (green), and 100 Myr (pink). As expected from Fig. 13, averaging over shorter time-scales (5–10 Myr) leads a smaller scatter and a better alignment with the one-to-one relation than averaging over longer time-scales. The RMSD introduced above (see equation 9) corresponds to the scatter with respect to this one-to-one line.

In the right-hand panel of Fig. 17, we plot the normalized RMSD as a function of the averaging time-scale. The MW, LMC-BC03, and LMC-BPASS simulations are shown in red, purple, and teal, respectively. The dashed, solid, and dotted (only shown for the MW) lines show the results for the SFR estimated from the intrinsic H α emission, the dust-corrected (via Balmer decrement with the optical depth–slope relationship given by equation 8 and the effective conversion factor discussed in Section 5.2) H α emission, and the observed H α emission. The time-scales that minimize the RMSD for the case of the dust-corrected H α SFR are indicated with the circles

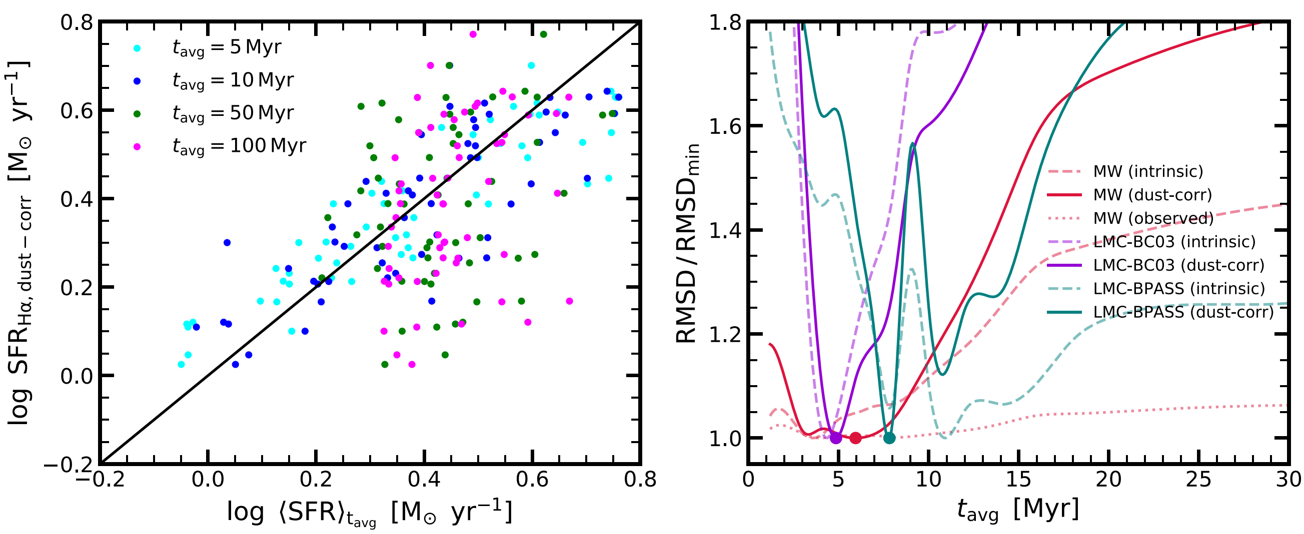

Figure 17. Inferring the time-scale of the H α SFR indicator. *Left:* Scatter plot of the dust-corrected H α SFR (${\rm SFR}_{{\rm H}\alpha,\,{\rm dust\text{-}corr}}$) versus the true SFR ($\langle{\rm SFR}\rangle_{t_{\rm avg}}$), averaged over 5 Myr (cyan), 10 Myr (blue), 50 Myr (green), and 100 Myr (pink). As expected from Fig. 13, averaging over shorter time-scales (5–10 Myr) leads a smaller scatter than averaging over longer time-scales. *Right:* Normalized RMSD (equation 9) between the true SFR of the simulation averaged over different time-scales $t_{\rm avg}$ and the SFR estimated from the intrinsic H α emission (dashed lines), the observed H α emission (dotted line; only shown for the MW case), and the dust-corrected (via Balmer decrement) H α emission (solid lines). The MW, LMC-BC03, and LMC-BPASS simulations are shown in red, purple, and teal, respectively. The solid dots indicate the minima for the dust-corrected H α SFR indicator, which minimizes the scatter in the one-to-one relation (as shown on the left). This averaging time-scale depends on the stellar population model, the star-formation variability, and the line-of-sight projection (Table 3).

Table 3. Star-formation time-scale ($t_{\rm avg,\,min}$) and 1σ scatter of the measured-to-time-averaged-true-SFR ratio ($\sigma_{\rm R}$) for the MW and LMC simulations. The following SFR indicators are shown from left to right: dust-corrected H α, intrinsic H α, observed (w/o dust correction) H α, and edge-on dust-corrected H α (instead of our default face-on project).

Simulation	H α (dust-corr)		H α (int)		H α (obs)		H α (dust-corr; edge-on)	
	$t_{\rm avg,\,min}$	$\sigma_{\rm R}$	$t_{\rm avg,\,min}$	$\sigma_{\rm R}$	$t_{\rm avg,\,min}$	$\sigma_{\rm R}$	$t_{\rm avg,\,min}$	$\sigma_{\rm R}$
MW	$5.9^{+2.3}_{-3.4}$	0.10	$3.6^{+2.7}_{-1.3}$	0.07	$4.0^{+16.0}_{-3.0}$	0.13	$7.7^{+2.4}_{-1.5}$	0.11
LMC-BC03	$4.9^{+0.6}_{-0.5}$	0.12	$4.5^{+0.5}_{-0.5}$	0.12	$7.5^{+0.7}_{-2.4}$	0.12	$4.7^{+0.5}_{-0.5}$	0.12
LMC-BPASS	$7.8^{+0.2}_{-0.3}$	0.17	$11.0^{+1.2}_{-0.7}$	0.18	$11.1^{+0.7}_{-0.5}$	0.14	$7.8^{+0.2}_{-0.3}$	0.18

and we tabulate these time-scales in Table 3. The uncertainties given in Table 3 are estimated by considering the RMSD 5 per cent above the its minimum.

As summarized in Table 3, the time-scale of the H α SFR indicator depends on several factors, including the star-formation variability itself (MW versus LMC), the amount of dust attenuation (face-on versus edge-on), and the stellar population model (BC03 versus BPASS). This time-scale also depends on the IMF, though we have fixed the IMF in our current investigation (see also Section 6.1). We find that, for the MW simulation, the SFR estimated from the intrinsic H α luminosity traces the SFR on a time-scale of $3.6^{+2.7}_{-1.3}$ Myr, which is shorter than the time-scale of $4.0^{+16.0}_{-3.0}$ Myr for the observed H α-based SFR (not corrected for dust), though the latter has a significant tail to much longer time-scales. This can be explained by the fact that the youngest stars are still embedded within molecular clouds, which leads to higher dust absorption of H α photons that trace those youngest stars. When correcting for dust, the tail towards long time-scales of observed H α-based SFR disappears. The numbers for the face-on and edge-on case are 5.9 and 7.7 Myr, respectively, indicating that the amount of dust attenuation plays an important role as well.

Comparing these results to the LMC simulations (both LMC-BC03 and LMC-BPASS), we find qualitatively similar trends, though there are quantitative differences. First, the adjustment of the SFR based on the intrinsic H α luminosity to the one based on the dust-corrected and observed H α luminosity is smaller. This is because there is less dust attenuation in the LMC simulations in comparison with the MW simulation. Secondly, the averaging time-scale for the intrinsic H α-based SFR is longer for the LMC simulation ($4.5^{+0.5}_{-0.5}$ Myr for the LMC-BC03 and $11.0^{+1.2}_{-0.7}$ Myr for the LMC-BPASS) with respect to the MW simulation ($3.6^{+2.7}_{-1.3}$ Myr). The difference in the LMC-BC03 can be explained by the larger fractional contribution of older stars (i.e. lower specific SFR), while the difference in LMC-BPASS model additionally stems from the fact that intermediate-age stars (10–100 Myr) in the BPASS model produce significantly more ionizing photons than the ones in the BC03 model (Appendix B). In summary, we find that H α traces the SFR on time-scales of 5–8 Myr.

This is overall consistent with quoted values in the literature. Flores Velázquez et al. (2021) found 5 Myr by convolving the SFHs of the FIRE simulation with the H α response function of the BPASS model (i.e. without radiative transfer). Similarly, using a family of variable SFHs drawn from a power spectrum density, Caplar & Tacchella (2019) quote values of 2–6 Myr, depending on the burstiness of the SFH itself. Haydon et al. (2020b) used an idealized hydrodynamical disc galaxy simulation without radiative transfer (no dust attenuation and scatter) and inferred an H α time-scale of $4.32^{+0.09}_{-0.23}$ Myr, which is close to our intrinsic time-scale (Table 3). Haydon et al. (2020a) revisited results from Haydon et al. (2020b) by quantifying the impact of dust extinction, and found that extinction mostly decreases the SFR tracer emission time-scale (factor of a few for H α). Observationally, correlating maps of different light tracers such as H α, CO, and 24 μm on spatially resolved scales to empirically constrain the giant molecular cloud lifecycle (see also Kruijssen et al. 2019; Chevance et al. 2020), Kim et al. (2021) found a duration of H α emitting phase of 5.5–8.9 Myr for nearby spiral galaxies, which is consistent with our dust-corrected time-scale estimates.

Finally, $\mathrm{SFR_{ind}}$ is not exactly equal to $\langle \mathrm{SFR}\rangle_{t_{\rm avg}}$ in the general case. Therefore, we now address the question: how well does the measured SFR match the true SFR averaged over $t_{\rm avg,\,min}$? Following Flores Velázquez et al. (2021), we investigate the scatter of the measured-to-time-averaged-true-SFR ratio ($R^{\rm ind}_{t_{\rm avg}} = \mathrm{SFR_{ind}}/\langle \mathrm{SFR}\rangle_{t_{\rm avg}}$) and provide in Table 3 the standard deviation of $\log R^{\rm ind}_{t_{\rm avg}}$ ($\equiv \sigma_{\rm R}$). We find $\sigma_{\rm R}$ for the dust-corrected H α-based SFR to be 0.10, 0.12, and 0.17 for the MW, LMC-BC03, and LMC-BPASS, respectively. The values for $\sigma_{\rm R}$ only marginally decrease when switching to the intrinsic H α-based SFR, highlighting that this scatter is caused by both the uncertainty of the H α-to-SFR conversion (Section 5.2) and the dust correction (Section 5.3).

6 LIMITATIONS AND FUTURE PROSPECTS

6.1 Current limitations and caveats

An important result regarding the H α-to-SFR conversion is the significant effect of the dust absorption of ionizing LyC photons produced by young stars. In the case of the MW simulation, $\sim$ 28 per cent of the LyC photons are absorbed by dust, $\sim$ 8 per cent ionize He I, $\sim$ 1 per cent ionize He II, $\sim$ 6 per cent escape the galaxy, implying that only about $\sim$ 57 per cent of the produced LyC photons are available for ionizing hydrogen. Although we discuss in Section 5.2 that the rather high dust absorption is consistent with observational estimates, we acknowledge here that – even with parsec-scale resolution – it remains challenging to resolve dust in ionized H II regions. While the present treatment is state-of-the-art, dust modelling in general is highly uncertain, especially considering complex multiscale effects such as spatially dependent grain size distributions and compositions, decoupling of dust and gas kinematics, and various physical processes impacting growth and destruction mechanisms that in principle affect dust attenuation law shapes (e.g. Draine 2011; Aoyama et al. 2018; McKinnon et al. 2018, 2019; Li, Narayanan & Davé 2019).

As described in Section 2, we do not model the effects of AGNs, both in regard to the hydrodynamics or the radiative transfer. AGNs are an important source of ionizing radiation, in particular near the central regions of some galaxies. Although we find a good agreement with the overall Balmer surface brightness profiles (Section 3), we do not judge the agreement in the centre as the consistency could be serendipitous. Obviously, it is of great interest to understand the impact of AGN feedback on the surrounding gas and how this could be detected in IFU data through broadened emission lines (e.g.

Förster Schreiber et al. 2014; Genzel et al. 2014). Along similar lines, we have not included X-ray binaries in the numerical model, though they are of interest for both changing the cooling function (e.g. Kannan et al. 2016) and as a production site for ionizing raditation (e.g. Schaerer, Fragos & Izotov 2019; Senchyna et al. 2020).

SPS models are the foundation for interpreting galaxy observations. They account for the light emitted by stars and the reprocessing of that light by dust, and some codes also include nebular emission (see reviews by Walcher et al. 2011; Conroy 2013). These SPS models have a number of assumed parameters that can alter the amount of ionizing flux significantly (e.g. Eldridge & Stanway 2012; Levesque et al. 2012; Stanway, Eldridge & Becker 2016), through stellar atmospheres (winds, opacities) and stellar evolution (mass-loss, rotation, binarity). Here, we have investigated how stellar binarity affects some of our conclusions by running the LMC simulation with the BC03 as well as the BPASS stellar models (Section 2). Changing the SPS has two effects. First, it changes the production rate of ionizing photons with stellar age (Appendix B). Secondly, it affects the strength and timing of radiative feedback, stellar winds, and supernova feedback, which are all modelled self-consistently. We show, among other things, that (i) the SFH is more variable in the LMC-BC03 simulation than in the LMC-BPASS model (Fig. 13); (ii) there is a higher helium absorption but a lower escape fraction of LyC photons in the LMC-BC03 model than in the LMC-BPASS model; and (iii) in the LMC-BC03 model H α traces the SFR on ∼5 Myr, while it is ∼8 Myr in the LMC-BPASS case (Fig. 17 and Table 3). In the future (see below), it will be of great interest to better understand how we can constrain the SPS model (by breaking degeneracies with, e.g. IMF, metallicity, and SFH) from galaxy integrated measurements that are based on combining UV-to-IR photometry with measurements of the Balmer (and possibly Paschen) emission lines.

Finally, we note that the stellar mass resolution of 2.8×10^3 $\mathrm{M}_\odot$ per particle is sufficient to resolve the SFH of the LMC and MW simulation. In a 5 Myr time bin, we will be able to resolve an SFR of 0.6×10^{-3} $\mathrm{M}_\odot\,\mathrm{yr}^{-1}$ with one particle. This implies that the median SFR of the LMC simulation is resolved with ∼66 (∼13) particles considering a time in of 5 Myr (1 Myr) time interval. Nevertheless, for the LMC (and lower mass dwarfs), stochastic sampling of the IMF will have interesting and important effects (e.g. Fumagalli, da Silva & Krumholz 2011; da Silva, Fumagalli & Krumholz 2014). In particular, regarding the H α-to-SFR conversion, even if a galaxy has a constant SFR, at low SFR the H α emission will fluctuate because of the fact that massive OB stars, which dominate the production of LyC photons, form rarely. In the limit of very low SFRs, these massive stars can be so rare that their number fluctuates significantly with time, leading to an additional source of stochasticity. This leads to an increase of scatter and also an overall bias to lower H α emission for a given SFR.

6.2 Future applications

The presented Balmer line (H α and H β) radiative transfer study of high-resolution MW-like and LMC-like galaxies is only the first step and will allow us to make further progress in several different directions in the future. As mentioned above, having broad-band UV-IR photometry in addition to the Balmer emission lines will allow us to tackle interesting questions related to the accuracy of SED modelling and degeneracies related to the SPS models. Therefore, we plan to expand our spectral coverage of synthetic observations to include stellar and dust continuum radiative transfer based on state-of-the-art pipelines (e.g. Camps & Baes 2015; Narayanan et al. 2021).

Along these lines, we would like to extend our spatially resolved MCRT framework to include metal ionization for self-consistent nebular line studies. This will allow us to address several interesting issues, including: (i) the selection efficiency of the DIG via the strength of the [S II] emission line; (ii) understanding how the DIG potentially biases strong-line gas-phase metallicity measurements (e.g. Sanders et al. 2017; Poetrodjojo et al. 2019); (iii) improved selection of star formation, AGN and shock regions in galaxies; and (iv) calibrations of ISM pressure and electron density diagnostics (e.g. Kewley, Nicholls & Sutherland 2019).

Employing our spatially resolved MCRT methodology with these aforementioned improvements will be key to understanding the physics of emission lines of and within galaxies both at low and high redshifts. In particular, we are currently working on zoom-in simulations based on the SMUGGLE-RT framework as part of the THESAN project (Kannan et al. 2021a, 2022; Garaldi et al. 2022; Smith et al. 2022), which are ideally suited for studying the high-redshift Universe. These and similar simulations will allow us to (i) better understand current and upcoming observations by being able to accurately estimate uncertainties and be aware of possible biases; and (ii) gain inspiration for new observational projects.

7 CONCLUSIONS

In this work, we shed new light on to the emission, absorption, and scattering of Balmer emission lines (H α and H β) in MW-like and LMC-like galaxies to better understand the importance of collisionally excited gas, emission of the DIG (including extraplanar emission), and connections between H α emission and SFRs. We perform a detailed radiative transfer analysis of high-resolution isolated MW and LMC simulations that include radiative transfer, non-equilibrium thermochemistry, and dust evolution. We confirm that the simulations produce realistic H α and H β radial and vertical surface brightness profiles that are consistent with observations of local MW-like and LMC-like galaxies (Figs 3 and 4). The main results and conclusions of this work are as follows:

(i) H α (and H β) photons are predominantly produced by recombination of ionized gas, which is ionized by LyC photons (Fig. 2). We also find that a small fraction (5–10 per cent) of the total Balmer emission stems from collisionally excited gas (Fig. 6) and an even smaller fraction (<2 per cent) from collisionally ionized gas.

(ii) Although different selection techniques lead to quantitatively different DIG fractions, we find that the observed DIG fraction is of the order of ~ 50 per cent, roughly consistent with observations (Fig. 9). Importantly, the intrinsic DIG fraction (i.e. before accounting for dust absorption and scattering) is a factor of 2–3 times lower because of dust attenuation effects. Furthermore, we show in Fig. 11 that the H α EW distribution is not easy to interpret because it is severely affected by spatial binning. We confirm that a value of EW(H α) = 14 Å seems to work well for selecting pure H II regions.

(iii) The extraplanar Balmer emission is produced *in situ* by ionizing photons emitted from the disc via radiative recombination (Fig. 12). Those ionizing photons must be transported through transparent pathways carved out by superbubbles or chimneys. Since the gas density is low at large scale heights, we classify all of this Balmer emission as being emitted from the DIG.

(iv) When converting the intrinsic (or dust-corrected) H α luminosity to an SFR, we find that a correction of $\sim 10-60$ per cent needs to be applied in order to account for the pre-absorption of LyC photons by dust ($f_{\mathrm{abs}} \approx 28$ per cent) and helium ($f_{\mathrm{He}} \approx 9$ per cent) and for the escape of LyC photons ($f_{\mathrm{esc}} \approx 6$ per cent; see Fig. 14).

This correction depends on the recent SFH and therefore cannot straightforwardly be applied in observations without further information. Effects related to H α emission by collisionally excited and ionized gas and related to older stars contribute at the 5 per cent level or less.

(v) The intrinsic H α can be well recovered (within 25 per cent) from the observed H α emission by applying the Balmer decrement method (see Fig. 16). We find that the nebular attenuation law depends on the amount of attenuation both on integrated and spatially resolved scales, and that more attenuated regions follow a shallower attenuation law (see equation 8 and Fig. 15).

(vi) The star-formation time-scale for the H α-based SFR indicator is 5–10 Myr (see Fig. 17 and Table 3). We quantify how the exact time-scale depends on the variability of the SFH (LMC versus MW), the stellar population model, and the amount of attenuation. It is important to consider this variation when measuring the 'burstiness' of star formation from, for example, the H α-to-UV ratio.

In the future, we will apply this framework to cosmological (zoom-in) simulations. Such studies will allow us to more accurately interpret spectroscopic data of high-redshift galaxies with the upcoming *James Webb Space Telescope*. Specifically, drawing from an improved understanding of the H α–SFR connection, we will be able to assess the spatially resolved stellar-mass growth and the regulation of star formation via time variability investigations.

ACKNOWLEDGEMENTS

We thank the referee for a thorough report that greatly improved this work. We thank Samir Salim for detailed comments; Ben Johnson, Diederik Kruijssen, and Ryan Sanders for insightful discussions; and Francesco Belfiore for sharing and discussing the results of the PHANGS-MUSE survey. This research made use of NASA's Astrophysics Data System (ADS), the arXiv.org preprint server, the Python plotting library `matplotlib` (Hunter 2007), and `astropy`, a community-developed core Python package for Astronomy (Astropy Collaboration 2013, 2018). ST is supported by the 2021 Research Fund 1.210134.01 of UNIST (Ulsan National Institute of Science & Technology) and by the Smithsonian Astrophysical Observatory through the CfA Fellowship. AS and HL acknowledge support for Program numbers *HST*-HF2-51421.001-A and *HST*-HF2-51438.001-A provided by NASA through a grant from the Space Telescope Science Institute, which is operated by the Association of Universities for Research in Astronomy, Incorporated, under NASA contract NAS5-26555. MV acknowledges support through NASA ATP 19-ATP19-0019, 19-ATP19-0020, 19-ATP19-0167, and NSF grants AST-1814053, AST-1814259, AST-1909831, AST-2007355, and AST-2107724. FM acknowledges support through the program 'Rita Levi Montalcini' of the Italian MUR. PT acknowledges support from NSF AST-1909933, NSF AST-2008490, and NASA ATP Grant 80NSSC20K0502. LVS acknowledges support from the NSF AST 1817233 and NSF CAREER 1945310 grants. Computing resources supporting this work were provided by the Extreme Science and Engineering Discovery Environment (XSEDE), at Comet through allocation TG-AST200007 and by the NASA High-End Computing (HEC) Program through the NASA Advanced Supercomputing (NAS) Division at Ames Research Center.

Funding for the Sloan Digital Sky Survey IV has been provided by the Alfred P. Sloan Foundation, the U.S. Department of Energy Office of Science, and the Participating Institutions. SDSS-IV acknowledges support and resources from the Center for High Performance Computing at the University of Utah. The SDSS website is www.sdss.org. SDSS-IV is managed by the Astrophysical Research Consortium for the Participating Institutions of the SDSS Collaboration including the Brazilian Participation Group, the Carnegie Institution for Science, Carnegie Mellon University, Center for Astrophysics | Harvard & Smithsonian, the Chilean Participation Group, the French Participation Group, Instituto de Astrofísica de Canarias, The Johns Hopkins University, Kavli Institute for the Physics and Mathematics of the Universe (IPMU) / University of Tokyo, the Korean Participation Group, Lawrence Berkeley National Laboratory, Leibniz Institut für Astrophysik Potsdam (AIP), Max-Planck-Institut für Astronomie (MPIA Heidelberg), Max-Planck-Institut für Astrophysik (MPA Garching), Max-Planck-Institut für Extraterrestrische Physik (MPE), National Astronomical Observatories of China, New Mexico State University, New York University, University of Notre Dame, Observatário Nacional / MCTI, The Ohio State University, Pennsylvania State University, Shanghai Astronomical Observatory, United Kingdom Participation Group, Universidad Nacional Autónoma de México, University of Arizona, University of Colorado Boulder, University of Oxford, University of Portsmouth, University of Utah, University of Virginia, University of Washington, University of Wisconsin, Vanderbilt University, and Yale University.

DATA AVAILABILITY

Raw data were generated by performing simulations at the NASA Pleiades computer. Derived data supporting the findings of this study are available from the corresponding author ST on request.

REFERENCES

Aguado D. S. et al., 2019, ApJS, 240, 23
Aoyama S., Hou K.-C., Hirashita H., Nagamine K., Shimizu I., 2018, MNRAS, 478, 4905
Astropy Collaboration, 2013, A&A, 558, A33
Astropy Collaboration, 2018, AJ, 156, 123
Baldwin J. A., Phillips M. M., Terlevich R., 1981, PASP, 93, 5
Barnes J. E., Wood K., Hill A. S., Haffner L. M., 2015, MNRAS, 447, 559
Barnes A. T. et al., 2021, MNRAS, 508, 5362
Belfiore F. et al., 2018, MNRAS, 477, 3014
Belfiore F. et al., 2019, AJ, 158, 160
Belfiore F. et al., 2022, A&A, 659, A26
Berman L., 1936, MNRAS, 96, 890
Blanton M. R. et al., 2005, AJ, 129, 2562
Blanton M. R., Kazin E., Muna D., Weaver B. A., Price-Whelan A., 2011, AJ, 142, 31
Bruzual G., Charlot S., 2003, MNRAS, 344, 1000 (BC03)
Bundy K. et al., 2015, ApJ, 798, 7
Byler N., Dalcanton J. J., Conroy C., Johnson B. D., 2017, ApJ, 840, 44
Byler N., Dalcanton J. J., Conroy C., Johnson B. D., Choi J., Dotter A., Rosenfield P., 2019, AJ, 158, 2
Calzetti D., 1997, AJ, 113, 162
Calzetti D., Kinney A. L., Storchi-Bergmann T., 1994, ApJ, 429, 582
Camps P., Baes M., 2015, Astron. Comput., 9, 20
Caplar N., Tacchella S., 2019, MNRAS, 487, 3845
Cardelli J. A., Clayton G. C., Mathis J. S., 1989, ApJ, 345, 245
Chabrier G., 2003, PASP, 115, 763
Charlot S., Fall S. M., 2000, ApJ, 539, 718
Cherinka B. et al., 2019, AJ, 158, 74
Chevallard J., Charlot S., Wandelt B., Wild V., 2013, MNRAS, 432, 2061
Chevance M. et al., 2020, MNRAS, 493, 2872
Choi J., Conroy C., Byler N., 2017, ApJ, 838, 159
Cid Fernandes R. et al., 2014, A&A, 561, A130
Conroy C., 2013, ARA&A, 51, 393
da Silva R. L., Fumagalli M., Krumholz M. R., 2014, MNRAS, 444, 3275

Decleir M. et al., 2019, MNRAS, 486, 743
Dopita M. A., Sutherland R. S., 2003, Astrophysics of the Diffuse Universe. Springer, Berlin
Draine B. T., 2011, ApJ, 732, 100
Driver S. P., Robotham A. S. G., Bland-Hawthorn J., Brown M., Hopkins A., Liske J., Phillipps S., Wilkins S., 2013, MNRAS, 430, 2622
Dwek E., 1998, ApJ, 501, 643
Eldridge J. J., Stanway E. R., 2009, MNRAS, 400, 1019
Eldridge J. J., Stanway E. R., 2012, MNRAS, 419, 479
Eldridge J. J., Stanway E. R., Xiao L., McClelland L. A. S., Taylor G., Ng M., Greis S. M. L., Bray J. C., 2017, PASA, 34, e058
Ellison S. L., Sánchez S. F., Ibarra-Medel H., Antonio B., Mendel J. T., Barrera-Ballesteros J., 2018, MNRAS, 474, 2039
Emami N., Siana B., Weisz D. R., Johnson B. D., Ma X., El-Badry K., 2019, ApJ, 881, 71
Emsellem E. et al., 2022, A&A, 659, A191
Faisst A. L., Capak P. L., Emami N., Tacchella S., Larson K. L., 2019, ApJ, 884, 133
Faucher-Giguère C.-A., Lidz A., Zaldarriaga M., Hernquist L., 2009, ApJ, 703, 1416
Ferrara A., Bianchi S., Dettmar R.-J., Giovanardi C., 1996, ApJ, 467, L69
Flores Velázquez J. A. et al., 2021, MNRAS, 501, 4812
Förster Schreiber N. M. et al., 2014, ApJ, 787, 38
Fumagalli M., da Silva R. L., Krumholz M. R., 2011, ApJ, 741, L26
Garaldi E., Kannan R., Smith A., Springel V., Pakmor R., Vogelsberger M., Hernquist L., 2022, MNRAS, 512, 4909
Genzel R. et al., 2014, ApJ, 796, 7
Groves B., Brinchmann J., Walcher C. J., 2012, MNRAS, 419, 1402
Guo Y. et al., 2016, ApJ, 833, 37
Haydon D. T., Fujimoto Y., Chevance M., Kruijssen J. M. D., Krumholz M. R., Longmore S. N., 2020a, MNRAS, 497, 5076
Haydon D. T., Kruijssen J. M. D., Chevance M., Hygate A. P. S., Krumholz M. R., Schruba A., Longmore S. N., 2020b, MNRAS, 498, 235
Hernquist L., 1990, ApJ, 356, 359
Hernquist L., 1993, ApJ, 409, 548
Hirashita H., Buat V., Inoue A. K., 2003, A&A, 410, 83
Hoyle F., Ellis G. R. A., 1963, Aust. J. Phys., 16, 1
Hunter J. D., 2007, Comput. Sci. Eng., 9, 90
Iglesias-Páramo J., Boselli A., Gavazzi G., Zaccardo A., 2004, A&A, 421, 887
Inoue A. K., Hirashita H., Kamaya H., 2001, ApJ, 555, 613
Iyer K. G. et al., 2020, MNRAS, 498, 430
Jo Y.-S., Seon K.-I., Shinn J.-H., Yang Y., Lee D., Min K.-W., 2018, ApJ, 862, 25
Kado-Fong E., Kim J.-G., Ostriker E. C., Kim C.-G., 2020, ApJ, 897, 143
Kannan R., Vogelsberger M., Stinson G. S., Hennawi J. F., Marinacci F., Springel V., Macciò A. V., 2016, MNRAS, 458, 2516
Kannan R., Vogelsberger M., Marinacci F., McKinnon R., Pakmor R., Springel V., 2019, MNRAS, 485, 117
Kannan R., Marinacci F., Vogelsberger M., Sales L. V., Torrey P., Springel V., Hernquist L., 2020, MNRAS, 499, 5732
Kannan R., Smith A., Garaldi E., Shen X., Vogelsberger M., Pakmor R., Springel V., Hernquist L., 2021a, preprint (arXiv:2111.02411)
Kannan R., Vogelsberger M., Marinacci F., Sales L. V., Torrey P., Hernquist L., 2021b, MNRAS, 503, 336
Kannan R., Garaldi E., Smith A., Pakmor R., Springel V., Vogelsberger M., Hernquist L., 2022, MNRAS, 511, 4005
Katz H. et al., 2019, MNRAS, 487, 5902
Kennicutt R. C., Jr, 1983, ApJ, 272, 54
Kennicutt R. C., Jr, 1998, ARA&A, 36, 189
Kewley L. J., Nicholls D. C., Sutherland R. S., 2019, ARA&A, 57, 511
Kim J. et al., 2021, MNRAS, 504, 487
Kim J.-h., Krumholz M. R., Wise J. H., Turk M. J., Goldbaum N. J., Abel T., 2013, ApJ, 779, 8
Kim J.-h., Wise J. H., Abel T., Jo Y., Primack J. R., Hopkins P. F., 2019, ApJ, 887, 120
Koyama Y. et al., 2015, MNRAS, 453, 879
Kreckel K., Blanc G. A., Schinnerer E., Groves B., Adamo A., Hughes A., Meidt S., 2016, ApJ, 827, 103
Kruijssen J. M. D. et al., 2019, Nature, 569, 519
Lacerda E. A. D. et al., 2018, MNRAS, 474, 3727
Law D. R. et al., 2016, AJ, 152, 83
Lee J. C. et al., 2009, ApJ, 706, 599
Levesque E. M., Leitherer C., Ekstrom S., Meynet G., Schaerer D., 2012, ApJ, 751, 67
Levy R. C. et al., 2019, ApJ, 882, 84
Li Q., Narayanan D., Davé R., 2019, MNRAS, 490, 1425
Ma X., Quataert E., Wetzel A., Hopkins P. F., Faucher-Giguère C.-A., Kereš D., 2020, MNRAS, 498, 2001
Mac Low M.-M., Ferrara A., 1999, ApJ, 513, 142
McKee C., 1989, in Allamandola L. J., Tielens A. G. G. M., eds, Proc. IAU Symp. 135, Interstellar Dust. Kluwer Academic Publishers, Dordrecht, p. 431
McKinnon R., Torrey P., Vogelsberger M., 2016, MNRAS, 457, 3775
McKinnon R., Torrey P., Vogelsberger M., Hayward C. C., Marinacci F., 2017, MNRAS, 468, 1505
McKinnon R., Vogelsberger M., Torrey P., Marinacci F., Kannan R., 2018, MNRAS, 478, 2851
McKinnon R., Kannan R., Vogelsberger M., O'Neil S., Torrey P., Li H., 2019, preprint (arXiv:1912.02825)
Marinacci F., Sales L. V., Vogelsberger M., Torrey P., Springel V., 2019, MNRAS, 489, 4233
Narayanan D., Conroy C., Davé R., Johnson B. D., Popping G., 2018, ApJ, 869, 70
Narayanan D. et al., 2021, ApJS, 252, 12
Nelson E. J. et al., 2016a, ApJ, 817, L9
Nelson E. J. et al., 2016b, ApJ, 828, 27
Nelson E. J. et al., 2021, MNRAS, 508, 219
O'Donnell J. E., 1994, ApJ, 422, 158
Oey M. S. et al., 2007, ApJ, 661, 801
Osterbrock D. E., Ferland G. J., eds, 2006, Astrophysics of Gaseous Nebulae and Active Galactic Nuclei, 2nd edn. University Science Books, Mill Valley, CA
Pellegrini E. W., Rahner D., Reissl S., Glover S. C. O., Klessen R. S., Rousseau-Nepton L., Herrera-Camus R., 2020a, MNRAS, 496, 339
Pellegrini E. W., Reissl S., Rahner D., Klessen R. S., Glover S. C. O., Pakmor R., Herrera-Camus R., Grand R. J. J., 2020b, MNRAS, 498, 3193
Peters T. et al., 2017, MNRAS, 466, 3293
Planck Collaboration XIII, 2016, A&A, 594, A13
Poetrodjojo H., D'Agostino J. J., Groves B., Kewley L., Ho I. T., Rich J., Madore B. F., Seibert M., 2019, MNRAS, 487, 79
Puglisi A. et al., 2016, A&A, 586, A83
Rahmati A., Pawlik A. H., Raičević M., Schaye J., 2013, MNRAS, 430, 2427
Rand R. J., Kulkarni S. R., Hester J. J., 1990, ApJ, 352, L1
Reynolds R. J., 1989, ApJ, 339, L29
Reynolds R. J., 1990, in Bowyer S., Leinert C., eds, Proc. IAU Symp. 139, The Galactic and Extragalactic Background Radiation. Kluwer Academic Publishers, Dordrecht, p. 157
Robitaille T., Rice T., Beaumont C., Ginsburg A., MacDonald B., Rosolowsky E., 2019, Astrophysics Source Code Library, record ascl:1907.016
Rosdahl J., Teyssier R., 2015, MNRAS, 449, 4380
Rosdahl J., Blaizot J., Aubert D., Stranex T., Teyssier R., 2013, MNRAS, 436, 2188
Rosdahl J. et al., 2018, MNRAS, 479, 994
Salim S., Narayanan D., 2020, ARA&A, 58, 529
Salim S. et al., 2016, ApJS, 227, 2
Salim S., Boquien M., Lee J. C., 2018, ApJ, 859, 11
Salpeter E. E., 1955, ApJ, 121, 161
Sanders R. L., Shapley A. E., Zhang K., Yan R., 2017, ApJ, 850, 136
Schaerer D., Fragos T., Izotov Y. I., 2019, A&A, 622, L10
Senchyna P., Stark D. P., Mirocha J., Reines A. E., Charlot S., Jones T., Mulchaey J. S., 2020, MNRAS, 494, 941
Shivaei I., Reddy N. A., Steidel C. C., Shapley A. E., 2015, ApJ, 804, 149
Smith A., Safranek-Shrader C., Bromm V., Milosavljević M., 2015, MNRAS, 449, 4336

Smith A., Ma X., Bromm V., Finkelstein S. L., Hopkins P. F., Faucher-Giguère C.-A., Kereš D., 2019, MNRAS, 484, 39
Smith A. et al., 2021, preprint (arXiv:2111.13721)
Smith A., Kannan R., Garaldi E., Vogelsberger M., Pakmor R., Springel V., Hernquist L., 2022, MNRAS, 512, 3243
Sparre M., Hayward C. C., Feldmann R., Faucher-Giguère C.-A., Muratov A. L., Kereš D., Hopkins P. F., 2017, MNRAS, 466, 88
Springel V., 2010, ARA&A, 48, 391
Springel V., Hernquist L., 2005, ApJ, 622, L9
Stanway E. R., Eldridge J. J., Becker G. D., 2016, MNRAS, 456, 485
Tacchella S. et al., 2015, ApJ, 802, 101
Tacchella S. et al., 2018, ApJ, 859, 56
Tacchella S., Forbes J. C., Caplar N., 2020, MNRAS, 497, 698
Thilker D. A., Braun R., Walterbos R. A. M., 2000, AJ, 120, 3070
Trayford J. W., Frenk C. S., Theuns T., Schaye J., Correa C., 2019, MNRAS, 483, 744
Tsai J. C., Mathews W. G., 1995, ApJ, 448, 84
Vale Asari N., Couto G. S., Cid Fernandes R., Stasińska G., de Amorim A. L., Ruschel-Dutra D., Werle A., Florido T. Z., 2019, MNRAS, 489, 4721
Veilleux S., Cecil G., Bland-Hawthorn J., 2005, ARA&A, 43, 769
Vogelsberger M., Marinacci F., Torrey P., Puchwein E., 2020, Nat. Rev. Phys., 2, 42
Walcher J., Groves B., Budavári T., Dale D., 2011, Ap&SS, 331, 1
Wang E., Lilly S. J., 2020, ApJ, 892, 87
Weinberger R., Springel V., Pakmor R., 2020, ApJS, 248, 32
Weingartner J. C., Draine B. T., 2001, ApJ, 548, 296
Weisz D. R. et al., 2012, ApJ, 744, 44
Westfall K. B. et al., 2019, AJ, 158, 231
Wilkins S. M. et al., 2020, MNRAS, 493, 6079
Wood K., Reynolds R. J., 1999, ApJ, 525, 799
Yang Y.-L. et al., 2020, ApJ, 891, 61
Zhang K. et al., 2017, MNRAS, 466, 3217
Zurita A., Rozas M., Beckman J. E., 2000, A&A, 363, 9

APPENDIX A: ADDITIONAL MAPS

A1 LMC maps

For completeness, we plot in Fig. A1 the maps of stellar mass, SFR, gas mass, and H α luminosity for the LMC-BC03 simulation.

A2 Effect of smoothing

Fig. A2 shows how different resolutions affect the visual appearance of the H α surface brightness maps. As discussed in Section 4.5, we focus on a resolution of 50 pc and 1.5 kpc, meaning that the FWHM of the PSF has a size of 50 pc and 1.5 kpc. This corresponds to roughly to resolution of MANGA and MUSE for nearby galaxies.

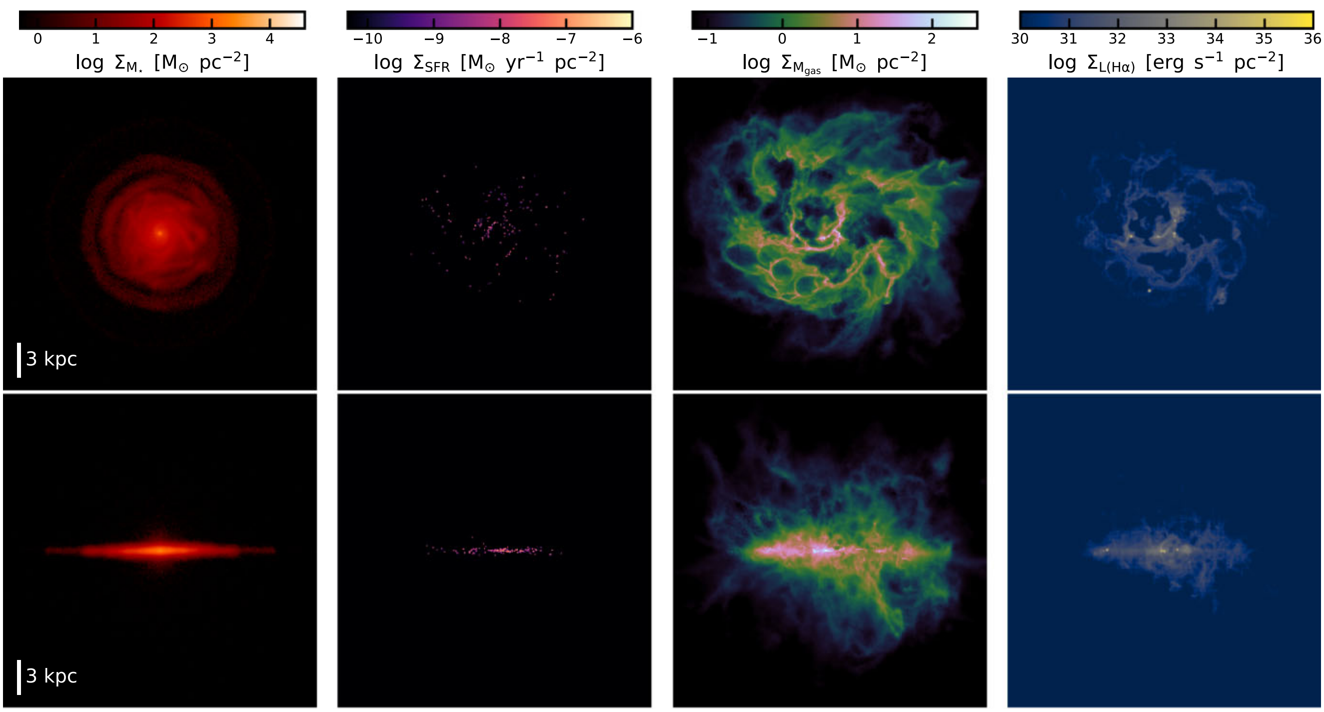

Figure A1. LMC-BC03 simulation at 713 Myr. This figure follows the same layout as Fig. 1: maps of stellar mass, SFR (averaged over the past 100 Myr), gas mass, and H α luminosity are shown from left to right. The stellar mass, SFR, and H α are smoothed by 50 pc in order to increase visibility. The top and bottom panels show face-on and edge-on projections, respectively. The dimensions of each map are 30 × 30 kpc (the ruler in the bottom left indicates 3 kpc).

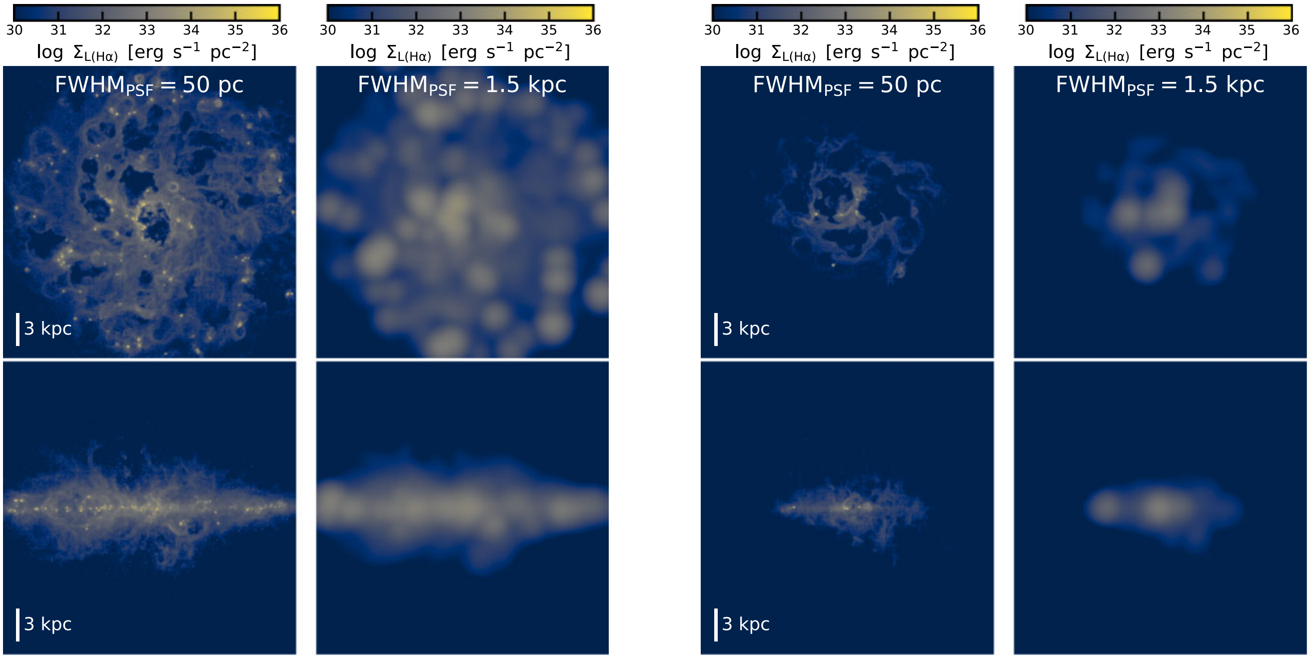

Figure A2. Effect of smoothing. We plot from left to right the H α surface brightness maps of the MW with a PSF FWHM of 50 pc, the MW with PSF FWHM of 1.5 kpc, the LMC-BC03 with PSF FWHM of 50 pc, and the LMC-BC03 with PSF FWHM of 1.5 kpc. The top panels show the face-on projections, while the bottom panels show the edge-on projections.

APPENDIX B: IONIZING RADIATION FROM DIFFERENT STELLAR POPULATION MODELS

The intrinsic production rate of H-ionizing Lyman continuum (LyC) photons of a galaxy depends on the IMF, the SFH, and the stellar population synthesis model. For the discussion here and throughout the paper, we fix the IMF to the Chabrier (2003) IMF with an upper mass limit of 100 $M_{\odot}$. We investigate the effect of the SFH and two stellar models: the Binary Population and Spectral Synthesis model (BPASS; Eldridge & Stanway 2009) and the Bruzual & Charlot (2003, denoted as BC03) model. Specifically, for each snapshot, we adopt the masses, ages, and metallicities of the stars of the MW and LMC simulations and convolve those with the BC03 and the BPASS models to compute the intrinsic production rate of LyC photons.

Fig. B1 investigates the stellar age dependence of the LyC photon production rate. Specifically, the left-hand panel plots the histogram of the number of LyC photons ($Q_{H\,I}$) as a function of stellar age, reflecting both the evolution of individual simple stellar populations (SSPs) as well as the SFH of the MW simulation (solid lines) and LMC simulation (dashed lines). As a reference, we also indicate the evolution of a BC03 SSP with an initial mass of 10^5 $M_{\odot}$ as a black line. The blue and pink lines show the BPASS and BC03 stellar synthesis models. Specifically, the solid line and shaded region mark the median and the 16–84th percentile across all simulation snapshots. The constancy beyond ~500 Myr is caused by the initialization of the simulation, where all old stars have a single age of 5 Gyr.

The left-hand panel of Fig. B1 clearly shows that young stars with ages of <10 Myr dominate production of LyC photons for both BC03 and BPASS. However, $Q_{\rm H\,I}$ declines faster with increasing stellar age for BC03 than for BPASS, implying that intermediate-age stars (10–200 Myr) contribute more significantly in BPASS to $Q_{\rm H\,I}$ than in BC03. After the main-sequence stars have died, post-AGB stars produce most of the ionizing flux in the older stellar populations (> 100 Myr), which explains the upturn at older ages for the BC03 models and the constancy in the case of the BPASS model (e.g. Byler et al. 2019).

Comparing the MW to the LMC simulation, we find a large (1–2 mag) normalization difference because of the higher stellar mass and SFR of the MW simulation than the LMC simulation (Table 1). This normalization difference is stellar age dependent mainly because of the different SFH. The ratio of younger versus older stars is larger for the MW than the LMC, which can be directly seen looking at the specific SFR (4×10^{-11} yr^{-1} for the MW versus 1×10^{-11} yr^{-1} for the LMC). An additional effect is the metallicity difference between the MW and LMC simulation, though this effect plays only a minor role (e.g. Byler et al. 2017; Choi, Conroy & Byler 2017).

The middle and right-hand panels of Fig. B1 show the contribution of intermediate (10–100 Myr) and old (>100 Myr) stars to $Q_{\rm H\,I}$ for the BPASS and BC03 models. For reference, the SFHs (SFR$_5$) are shown as orange lines, linearly rescaled by a factor of $0.1/\langle{\rm SFR}\rangle$ (see Table 1 for the MW and LMC values of $\langle{\rm SFR}\rangle$). For the SFH of the MW (middle panel), we find that in the case of BC03 the contribution to $Q_{\rm H\,I}$ of both intermediate and old stars is negligible with 0.6 per cent and 1.8 per cent, respectively. In the case of BPASS, the fractional contribution of intermediate-age stars is significant with 7^{+8}_{-3} per cent, while the contribution of old stars remains low (1.6 per cent). The contribution fraction of intermediate-age stars peaks (up to ~ 20 per cent) shortly after a burst of star formation.

The right-hand panel of Fig. B1 shows the results for the SFH of the LMC. As discussed in Section 5.1, the SFH is more variable for the LMC than the MW, i.e. there are periods in the SFH of the LMC where the SFR$_5$ is $<10^2$ $M_{\odot}$ yr^{-1}, typically proceeding a burst of star formation. In these phases of little-to-no star formation, the LyC production rate of young stars is very low (see also extended

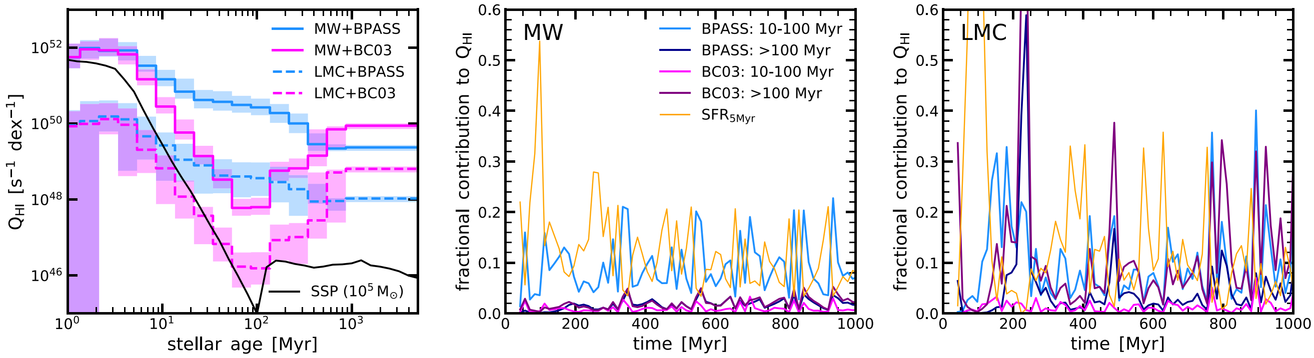

Figure B1. Stellar population dependence of the H-ionizing Lyman continuum (LyC) photon production rate. *Left*: The histogram shows the number of LyC photons as a function of stellar age, reflecting both the evolution of individual simple SSPs as well as the SFH of the MW simulation (solid lines) and LMC simulation (dashed lines). For reference, the black solid line marks the evolution of a BC03 SSP with an intial mass of 10^5 $M_{\odot}$. The blue and pink lines show the BPASS (Eldridge & Stanway 2009) and BC03 (Bruzual & Charlot 2003) stellar synthesis models. Specifically, the solid line and shaded region mark the median and the 16–84th percentile across all simulation snapshots. The constancy beyond ∼500 Myr is caused by the initialization of the simulation, where all old stars have a single age of 5 Gyr. *Middle* and *right*: Fractional contribution of older stars to the H-ionizing LyC flux emission as a function of time for the MW SFH (middle panel) and LMC SFH (right-hand panel). The pink and purple (light and dark blue) lines indicate the fraction of LyC photons that stem from 10–100 Myr and >100 Myr old stars in the BC03 (BPASS) models. The orange curve shows the normalized SFR averaged over 5 Myr. For the SFH of the MW simulation, we find that LyC photons are mainly produced by young stars (<10 Myr old stars) both in BC03 and BPASS models, though in the BPASS model intermediate-age stars (10–100 Myr) contribute more significantly (∼ 10 per cent) to the ionizing budget than in the BC03 model. The contribution fraction of intermediate-age stars peaks (up to ∼ 20 per cent) shortly after a burst of star formation. For the LMC SFH, the contribution of intermediate-age (and even older stars) stars varies more and peaks at larger values.

percentiles to low $Q_{\rm H\,I}$ values in the left-hand panel), leading to a boost in the relative contribution of intermediate and old stars. Specifically, in the BC03 case, we find a median contribution from old stars of 7^{+12}_{-4} per cent, but with short phases where the contributions amount to more than 30 per cent. Intermediate-age stars still only contribution on the level of ∼ 1 per cent. For the BPASS model, the situation is flipped: intermediate-age stars contribute more prominently with 8^{+10}_{-5} per cent, while the contribution from old stars is smaller (2^{+6}_{-1} per cent).

In summary, even when just studying the production rate of H-ionizing LyC photons without any radiative transfer effects, we see that changes in the stellar models (BC03 versus BPASS) and the SFH can lead to drastically different outcomes regarding the contribution of older stellar populations to the ionizing flux (see also, e.g. Choi et al. 2017; Rosdahl et al. 2018; Ma et al. 2020).

This paper has been typeset from a TEX/LATEX file prepared by the author.